



ECMWF Newsletter



Number 146 – Winter 2015/16

European Centre for Medium-Range Weather Forecasts
Europäisches Zentrum für mittelfristige Wettervorhersage
Centre européen pour les prévisions météorologiques à moyen terme

Reducing systematic errors in cold-air outbreaks
.....

A new grid for the IFS
.....

Diagnosing flow-dependent forecast reliability
.....

ECMWF's new data decoding software ecCodes
.....

© Copyright 2016

European Centre for Medium-Range Weather Forecasts, Shinfield Park, Reading, RG2 9AX, England

Literary and scientific copyright belong to ECMWF and are reserved in all countries. This publication is not to be reprinted or translated in whole or in part without the written permission of the Director-General. Appropriate non-commercial use will normally be granted under condition that reference is made to ECMWF.

The information within this publication is given in good faith and considered to be true, but ECMWF accepts no liability for error or omission or for loss or damage arising from its use.

CONTENTS

EDITORIAL

Exciting times 1

NEWS

Alan Thorpe’s legacy at ECMWF 2
 Forecasting flash floods in Italy 3
 Forecast performance 2015 5
 Tropical cyclone forecast performance 7
 Monitoring the 2015 Indonesian fires 8
 Visualising data using ecCharts: a user perspective 9
 Forecasts aid flood action in Peru during El Niño 10
 Calibrating river discharge forecasts 12
 CERA-20C production has started 13
 Migration to new ECMWF website is complete 15
 Software updates in preparation for model cycle 41r2 16

METEOROLOGY

Reducing systematic errors in cold-air outbreaks 17
 A new grid for the IFS 23
 Using ensemble data assimilation to diagnose flow-dependent forecast reliability 29

COMPUTING

ECMWF’s new data decoding software ecCodes 35

GENERAL

TAC Representatives, Computing Representatives and Meteorological Contact Points 40
 ECMWF Council and its committees 41
 ECMWF Calendar 2016 42
 Contact information 42
 ECMWF publications 43
 Index of newsletter articles 44

PUBLICATION POLICY

The *ECMWF Newsletter* is published quarterly. Its purpose is to make users of ECMWF products, collaborators with ECMWF and the wider meteorological community aware of new developments at ECMWF and the use that can be made of ECMWF products. Most articles are prepared by staff at ECMWF, but articles are also welcome from people working elsewhere, especially those from Member States and Co-operating States. The *ECMWF Newsletter* is not peer-reviewed.

Editor: Georg Lentze

Typesetting and Graphics: Anabel Bowen with the assistance of Simon Witter.

Cover image: NASA Worldview (<https://earthdata.nasa.gov/labs/worldview/>)

Any queries about the content or distribution of the *ECMWF Newsletter* should be sent to Georg.Lentze@ecmwf.int
 Guidance about submitting an article is available at www.ecmwf.int/en/about/news-centre/media-resources

CONTACTING ECMWF

Shinfield Park, Reading, Berkshire RG2 9AX, UK
 Fax: +44 118 986 9450
 Telephone: National 0118 949 9000
 International +44 118 949 9000
 ECMWF website: www.ecmwf.int

Exciting times

Three weeks into my role as Director-General, I am delighted at the opportunity to extend my best wishes for 2016 to all readers of the Newsletter.

2016 is set to be another exciting year for ECMWF. One of the first highlights will be the operational implementation of our new model cycle in March, taking the horizontal resolution to 9 km for high-resolution forecasts and 18 km for ensemble forecasts, and making full use of our new cubic-octahedral grid. We will also be finalising our next Strategy. It will guide the Centre’s direction for the next decade, strengthening the role of the ensemble approach and formalising our move to an Earth system model, including the atmosphere, ocean, land and sea ice.

Delivering our research and forecast objectives, and hosting the largest meteorological data archive in the world, has its challenges. This year we need to agree a location for our next supercomputer, with sustainability a key consideration. The externally funded projects of our Scalability Programme will produce the first examples of new code developments aiming to achieve maximum computing and energy efficiency.

After such an atypical El Niño year and with the societal importance of meteorology becoming increasingly visible, we have to recognise the size of our responsibility. The size of the challenge justifies the efforts that we, with our Member and Co-operating States, our partners at the WMO and academia at large, put into advancing weather science and raising the bar of forecast quality.

We will continue our collaborative work to provide authoritative environmental information, not least through the EU’s Copernicus programme.

I feel privileged to be leading such a talented team of experts. I would also like to thank my predecessor, Professor Alan Thorpe, for bringing me into his team and sharing his inspiring expertise. His collaborative way of working is now allowing for a smooth transition, for which we are all grateful.

I look forward to engaging with you through our busy programme of publications, workshops and training sessions and at international conferences.

Florence Rabier
 Director-General



Florence Rabier was Director of ECMWF’s Forecast Department from October 2013 to December 2015. You can read more about her background and career on ECMWF’s website at <http://www.ecmwf.int/en/about/media-centre/news/2015/ecmwf-appoints-new-director-general>.

Alan Thorpe's legacy at ECMWF

GERHARD ADRIAN
(ECMWF Council President)

On 31 December 2015, Alan Thorpe relinquished the post of Director-General of ECMWF after four and a half years. During that time, he helped the Centre to maintain its world-leading position in global medium-range numerical weather prediction and to enhance its Earth system prediction capabilities for the benefit of its Member States.

Alan is a physicist by training and, for many years, he was a Professor of Meteorology at the University of Reading. In 1999, he became the Director of the Hadley Centre for Climate Prediction and Research and subsequently the founding Director of the UK's National Centre for Atmospheric Science. In 2005, he took up the post of Chief Executive of the UK's Natural Environment Research Council, and from there he moved to ECMWF. Alan's background meant he was well placed to tackle the multiple organisational and scientific challenges that faced the Centre when he took up his post in July 2011.

At that time, ECMWF's Strategy 2011–2020 had just been adopted. The Strategy notes that ECMWF's new Convention provides the Centre with fresh opportunities, such as developing third-party activities. It foresees that, by 2020, routine atmospheric composition forecasts and a much-improved climate reanalysis spanning the 20th century will be available. And it warns of the need to adapt to changing supercomputer architectures.

New activities

Under Alan's leadership, decisive progress has been made on all these fronts. In a major development, on 11 November 2014 Alan signed an agreement in Brussels for ECMWF to manage the EU-funded Copernicus Climate Change and Atmosphere Monitoring Services, C3S and CAMS. Since then, a new Copernicus Services Department has been created, CAMS has become fully operational, and the development of C3S is making rapid progress.

ECMWF has also produced ERA-20C, an atmospheric reanalysis spanning the entire 20th century, and it is now producing CERA-20C, a new reanalysis in which ocean and atmospheric observations are assimilated simultaneously. This work aims to produce a comprehensive estimate of the evolution of the Earth system in the 20th century.

These are examples of EU-funded work which will benefit all of ECMWF's Member and Co-operating States.

The need to adapt ECMWF's forecasting code to tomorrow's massively parallel supercomputer architectures was high on Alan's agenda from the start. A Scalability Programme was launched in 2013 and is now well under way. It is a deeply collaborative project, whose results will be made available to all national meteorological services in the Member and Co-operating States. Today ECMWF co-ordinates the EU-funded ESCAPE project and is a key player in a number of related projects.

Successful forecasts

During Alan's time as Director-General, the overall performance of operational forecasts continued to improve, as measured by a standard set of headline scores. There were also some widely noted successful forecasts of severe weather.

In 2012, ECMWF's forecasts provided the earliest indication of Hurricane Sandy's path. The Integrated Forecasting System predicted the landfall of 'Superstorm Sandy' on the US East Coast seven days in advance. In 2015, the Centre made international media headlines again after correctly predicting, earlier than other models, that Hurricane Joaquin would not make landfall in the USA.

Organisational change

On the organisational front, Alan demonstrated his managerial skills by successfully instituting major changes. In July 2013, the Operations Department was split into the Forecast and Computing Departments to provide a clearer focus for some of the Centre's key activities, such as evaluating forecast skill.



Alan Thorpe. Alan was ECMWF's Director-General from July 2011 to December 2015.

Collaboration was a major theme, with Alan driving forward closer ties with the World Meteorological Organization as well as with national meteorological services in the US and China. His leadership of the first World Weather Open Science Conference in 2014 helped to establish the research agenda in weather science for the years to come. Four new Member States joined ECMWF during Alan's term: Iceland, Slovenia, Serbia, and (from 1 January 2016) Croatia.

A single figure gives a sense of the scale of the Centre's transformation under Alan: by December 2015, the number of staff (including consultants) had gone up by 23 per cent, from 248 when he started to 304 when he left.

Alan and the Council

Over the last five years, the pace of change at the Centre has accelerated and this has not always been easy for Council delegates to accept. This is true in particular of Alan's initiative to closely involve ECMWF in the EU's Copernicus Programme. As members of national meteorological services, we have tended to regard ECMWF as 'our' Centre while perhaps neglecting our wider role as representatives of the Member States, most of which are part of the EU.

This development, driven by Alan's initiatives, convinced us of the need to reassess the role of national

meteorological services in Europe, their relationship with European intergovernmental organisations, and their need to cooperate and to complement each other. Developing our views on these issues will support the creation of clearer interfaces between the Centre, its Member States, their national meteorological services and the European Union.

Alan's vision

Above all, Alan provided a vision for

the Centre within which the expansion of its activities and the organisational changes made eminent sense. He tirelessly made the case for an Earth system approach in the service of environmental prediction; seamless prediction across timescales; ensemble forecasting so that we can be specific about the confidence we can have in forecasts; and the need to bring the weather forecasting and climate prediction communities together to achieve all this.

His main legacy is that, as he leaves his post, ECMWF is prepared for its next 40 years with its globally-recognised role in research and numerical weather prediction at its heart. In addition, it is serving the Member States to help provide vitally important environmental information services, providing meteorological research data and databases and contributing to advancing the science and technology of weather prediction using an ensemble and Earth system approach.

Forecasting flash floods in Italy

**LINUS MAGNUSSON,
CALUM BAUGH,
FLORENCE RABIER,
FEDERICO GRAZZINI**
(ARPA-SIMC, Bologna, Italy)

After the very warm summer in southern Europe, the autumn brought a series of severe flash floods along the French and Italian coasts. On 13 September 2015, the Emilia-Romagna region in north-western Italy was hit by a convective storm. The severe weather caused flash floods in the north-west Apennines and record discharges for the Nure and Ceno rivers as well as the Trebbia, the largest river in the region. The precipitation was generated by a single V-shaped mesoscale convective system (MCS), which formed upstream of the Apennines in a warm and humid upper-level south-westerly flow. The persistence of the low-level convergence over the Ligurian Sea maintained the convective system and it was almost stationary for 12 hours. The precipitation intensity was extreme, with four stations recording more than 110 mm/hour and almost 10 stations recording more than 80 mm/hour during the most intense phase.

Ten weather stations which are part of a high-density regional network recorded more than 250 mm/24 hours and three stations more than 300 mm/24 hours. Relying on WMO exchange observations alone without this regional input, the evaluation of ECMWF's forecasts would have missed this event. An ongoing project at ECMWF aims to collect data from national high-

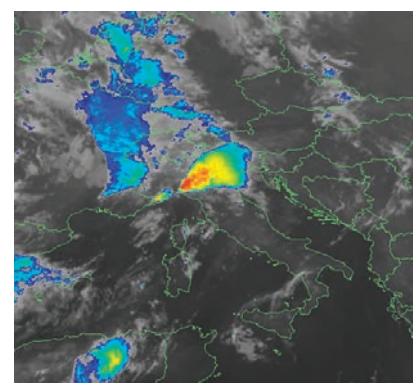


Farini village after the Nure stream flood. The Nure stream rose to a record level of about 5 metres. (Photo: Federico Grazzini)

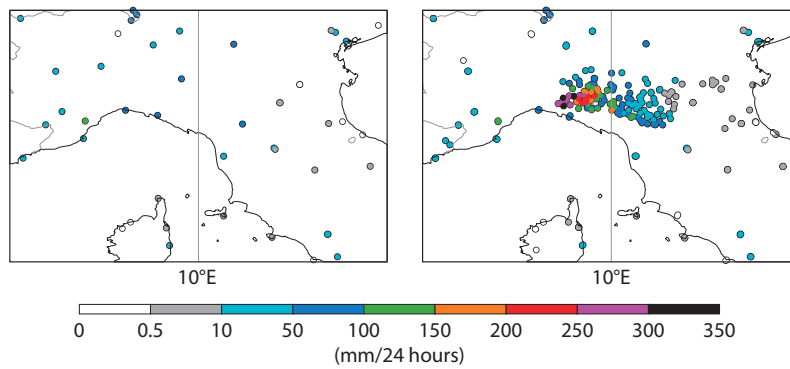
density networks to increase the quality of verification work and better support model development.

Forecasts

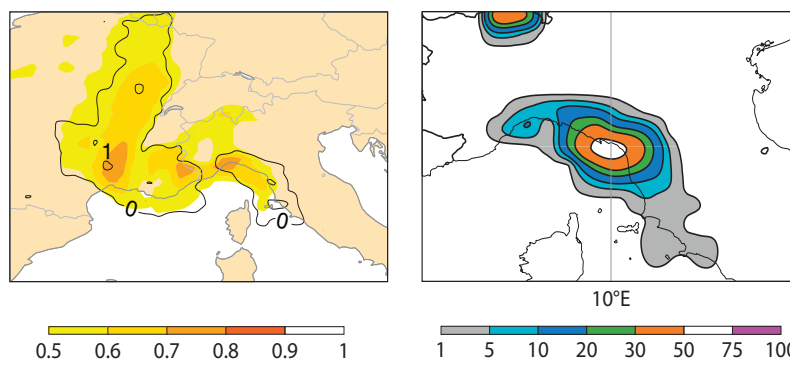
The Extreme Forecast Index (EFI) and Shift of Tails (SOT) from 9 September (4 to 5 days before the event) indicated the potential for extreme precipitation along the coasts of north-western Italy and southern France on 13 September. An ensemble forecast (ENS) relatively close to the event (from 12 September 12 UTC) put the highest probabilities of more than 100 mm/24 hours along the coast, while further inland, in the flash flood region, the predicted probabilities were lower. The HRES forecast from the same time gave a similar picture as the ensemble with the main precipitation over sea (not shown).



Satellite precipitation image. MSG-3 satellite enhanced infrared picture showing the V-shaped system in its mature phase at 00 UTC on 14 September.



Twenty-four-hour precipitation accumulation. Observations for 13 September 06 UTC to 14 September 06 UTC from WMO exchange (left) and including some regional network stations (right).



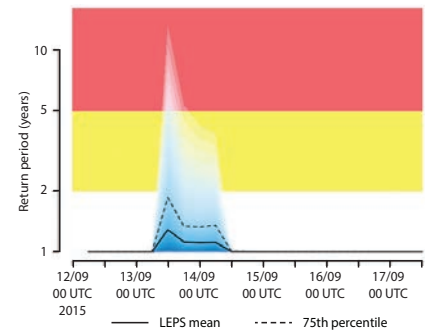
ECMWF forecasts for 13 September. EFI forecast (shading) and SOT forecast (contours) from 9 September 00 UTC (left) and ENS forecast from 12 September 12 UTC of probabilities of more than 100 mm/24 hours (right).

In the Copernicus Emergency Management Service – Early Warning System (Floods), formerly known as EFAS, additional products targeting flash floods are produced using the Enhanced Runoff Index based on Climatology (ERIC) method. Ensemble precipitation forecasts are taken from COSMO-LEPS and combined with soil moisture forecasts from the LISFLOOD hydrological model to estimate the amount of surface runoff. COSMO-LEPS is a limited-area ensemble provided by ARPA-ER SIMC (Italy) that uses the global ECMWF ensemble for initial and boundary conditions. For the flash flood event in Emilia-Romagna the ERIC forecast on 12 September 2015 00 UTC predicted only a low probability of major flash flooding within the affected area. A flood forecast for a point on the upper part of the River Trebbia (where the maximum precipitation was observed) indicated a 15% risk of exceeding a five-year return period, a relatively low but non-negligible probability. The large-scale atmospheric flow was captured in ECMWF’s medium-

range forecasts (even up to a week in advance) but the severe mesoscale convective system was missed even by the shortest-range HRES and ENS forecasts. COSMO-LEPS had a few members with a precipitation pattern similar to the observed one, but the resulting probability was low. The low probability was due to the local nature of the convective storm and the fact that only a few members predicted intense precipitation in the right place.

Outlook

It is anticipated that these events will be better simulated with higher model resolution, and that additional observations of moisture over the sea, such as data from the Meteosat Third Generation (MTG) programme, will produce better initial condition estimates. This should in turn improve precipitation and flood forecasts. However, small differences between forecasts and outcomes in the position of convective cells may still lead to relatively low probabilities from the ensemble forecasts, and post-processing of the raw data might still be needed.



Copernicus forecast for 12 to 17 September.

Copernicus probabilistic flash flood return period forecast for a point on the River Trebbia from 12 September 12 UTC. The blue-shaded area shows the predicted probability distribution of an event with a return period of more than a year for 6-hour intervals. According to the forecast, there is a 24% chance of an event with a return period of more than 2 years and a 15% chance of an event with a return period of more than 5 years in a 6-hour interval on 13 September.

Forecast performance 2015

**THOMAS HAIDEN,
TIM HEWSON,
MARTIN JANOUSEK,
DAVID RICHARDSON**

ECMWF maintains a comprehensive range of verification statistics to evaluate the accuracy of its forecasts. Each year, a summary of verification results is presented to ECMWF's Technical Advisory Committee (TAC). Their views about this year's performance of the operational forecasting system are given in the box.

The overall performance of the operational forecasts is summarised using a set of headline scores endorsed by the TAC, which highlight different aspects of forecast skill. Upper-air performance of the high-resolution forecast (HRES) in the extra-tropics is monitored through the anomaly correlation of 500 hPa geopotential. The most recent upgrade to the Integrated Forecasting System (IFS cycle 41r1) in May 2015 led to an increase in HRES skill relative to ERA-Interim, which is used as a reference to reduce the effect of variations in atmospheric predictability. In the first figure, which shows 12-month running averages, the effect of the upgrade just starts to be visible in the running averages centred on the first few months of 2015. Other minor fluctuations, such as the drop in relative skill in 2014, can be attributed to the fact that not all of the variations

in predictability are compensated for by the reference ERA-Interim forecast. An alternative benchmark is forecasts from other global centres. These confirm that ECMWF is maintaining its lead both for the HRES and the ENS.

Improvements in forecasts of 850 hPa vector wind in the tropics can be seen from verification against radiosondes. Due to an increase in analysis and forecast activity, verification against model analysis shows an improvement in terms of anomaly correlation but not root-mean-square error (RMSE).

While the non-systematic component of the 2 m temperature error in Europe has further decreased, the summer night-time positive bias at mid- to high latitudes has increased. Resolution of the issue requires the model to cool more strongly near the surface at night. However, implementation of such a change will depend on whether improvements in the representation of wintertime low cloud can be achieved, since its underestimation leads to a negative bias in night-time temperatures in winter, which would be further increased by stronger near-surface cooling.

The supplementary headline score that addresses ENS skill for precipitation is shown in the second figure. It can be seen that there have been improvements after the pronounced resolution-related increase in 2010. The resolution upgrade from 32 km to

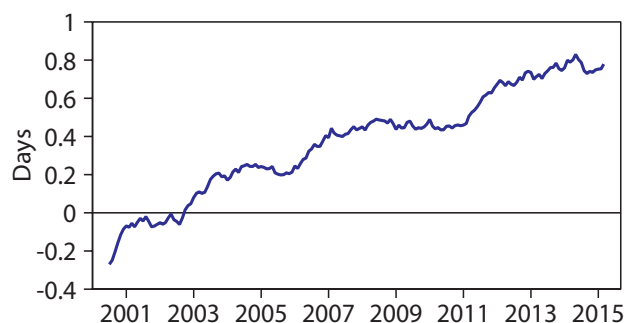
18 km for the ENS scheduled for 2016 is expected to lead to another noticeable increase in skill.

Forecasts of tropical cyclones have improved, with position and speed errors reaching their lowest values so far both for the HRES and ENS. Tropical cyclone intensity, which is still an issue especially for smaller-scale systems, is expected to improve in the ENS in 2016 as a result of the higher resolution.

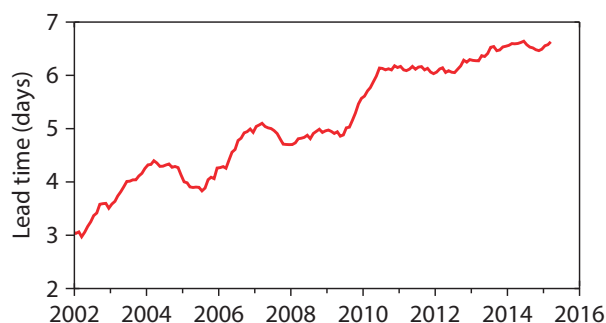
Wave forecast skill has increased with respect to both wave height and peak period, allowing ECMWF to maintain its lead compared to other global wave forecasting systems.

Predictability on the seasonal timescale benefitted from a strong El Niño, which started to develop in 2015 and which was well forecast by System 4. The warm anomaly in central and southern Europe during summer was qualitatively predicted. However, neither its magnitude nor the concurrent cold anomaly in northern Europe were fully captured.

ECMWF's IFS output has also been verified separately in many European countries. Most users focussed on HRES forecasts up to 48 hours, which they compared with limited-area model (LAM) output. Among the key observations was a persistent under-prediction of the diurnal temperature range in the HRES in clear, calm conditions, and an under-prediction bias for 10 m



Skill of the HRES relative to the ERA-Interim forecast. Results for geopotential at 500 hPa in the northern hemisphere extra-tropics show that the relative skill has continued to increase in recent years. The chart shows differences between HRES and ERA-Interim 12-month running average values of the forecast range at which the anomaly correlation drops below 80%.



Probabilistic skill of the precipitation forecast. Results for the northern hemisphere extra-tropics show that the skill of the ENS in predicting 24-hour precipitation totals has continued to increase since 2012. The computation of skill is based on the continuous ranked probability skill score (CRPSS). The chart shows 12-month running average values of the forecast range at which the CRPSS drops below 0.1.

wind speed in mountain areas.

It was also noted that the IFS under-predicts the frequency of large point rainfall (which can be addressed by situation-dependent post-processing), and that forecast skill for solar radiation and cloud cover becomes increasingly important as solar cell usage expands. Feedback provided by Member and Co-operating States is greatly appreciated as it helps to improve future model versions.

The complete set of annual results is available in ECMWF Tech. Memo. No. 765 on 'Evaluation of ECMWF forecasts, including 2014-2015 upgrades', downloadable from <http://www.ecmwf.int/en/research/publications>. This document presents

recent verification statistics and evaluations of ECMWF forecasts (including weather, waves and severe weather events) along with information about changes to the data assimilation/forecasting and post-processing systems. The performance of the monthly and seasonal forecasting systems is also assessed.

The following are other sources of information about verification and forecasting system changes:

- Verification pages on the ECMWF web server are regularly updated. Links to them can be found at: <http://www.ecmwf.int/en/forecasts/charts>
- Interactive plots showing inter-comparisons of global model

forecast skill can be found on the WMO Lead Centre for Deterministic Forecast Verification (WMO-LCDNV) web page at:

<http://apps.ecmwf.int/wmolcdnv/>

- All IFS forecasting system cycle changes since 1985 are described at: <http://www.ecmwf.int/en/forecasts/documentation-and-support/changes-ecmwf-model>
- Member States' reports on verification can be found at: http://www.ecmwf.int/search/elibrary?secondary_title=green_book_2015

Assessment of ECMWF's Technical Advisory Committee, 15–16 October 2015

With regard to its overall view of the performance level of forecasts of the ECMWF operational forecasting system, the Committee:

- congratulated ECMWF on maintaining its world-leading position in medium-range forecasting and encouraged ECMWF to maintain this lead;
- noted with satisfaction the continuous improvement compared to benchmark systems of headline scores for HRES and ENS as well as other scores;
- acknowledged the quality, timeliness and accuracy of the up-to-one-week-ahead forecast by ECMWF of many high-impact weather events; welcomed the work done on verifying extreme events in the framework of potential economic value (PEV), results showing clearly the value of the ensemble for relatively large-scale events such as windstorms and associated impacts;
- appreciated and encouraged ECMWF efforts to develop new measures of skill targeted at supporting decision-making for end users in high-impact situations in the medium range;
- learned with great interest of the work on diagnostics, especially with a view to getting useful predictive diagnostics for severe weather (CAPE-shear); additions in cycle 41r1 of new parameters (precipitation types including freezing rain, precipitation rates, visibility) were highly appreciated; work on systematic regime transition errors was also appreciated and its continuation is welcomed for forecasters to better understand model behaviour;
- encouraged ECMWF to consider reinstating the executive summary of feedback on performance from Member States' reports on verification, user meetings and forecaster user wiki pages in the discussion on performance;
- noticed that 10 m wind and night-time temperature biases over land are potential areas for exchange with LAM developers having experienced similar problems; appreciated that some of the overestimation in the occurrence of light rain events was corrected when the revised cloud scheme was introduced;
- encouraged further work showing the respective information brought by the high-resolution deterministic forecast and the ensemble;
- noted with satisfaction the operational implementation of cycle 41r1 after very extensive testing; welcomed the very condensed overview of impacts offered by the scorecard, and encouraged ECMWF to develop a representation of how the e-suite would impact headline scores had it been in operations;
- noticed some negative effects of changes to the land sea mask (LSM) representation on summer-time temperature forecasts at some locations, and encouraged ECMWF to further consider revisions of this LSM representation.

Tropical cyclone forecast performance

FERNANDO PRATES

Tropical cyclone (TC) forecast performance has been evaluated in model cycle 41r1 of the Integrated Forecasting System (current operational forecasting system) and compared with the previous cycle 40r1 (operational until 12 May 2015). Overall, the impact of the model upgrade on the predicted position and intensity (minimum surface pressure) of TCs is positive. There is a small reduction in mean position errors from day 5. The intensity bias is smaller than in the previous cycle from analysis time to day 5 but larger thereafter.

At the longer range, where forecasts in model cycle 41r1 tend to predict storms that are too intense, the differences between the two cycles are statistically less significant than at the shorter range, due to small sample sizes. Experiments carried out in the past suggest that the predicted intensity of TCs is sensitive to changes

in physical parametrizations and to ocean–atmosphere coupling. ECMWF’s high-resolution forecasts (HRES) are not produced using a coupled model. HRES forecasts are also slow to respond to rapid changes in the strength of TCs, which may lead to phase errors.

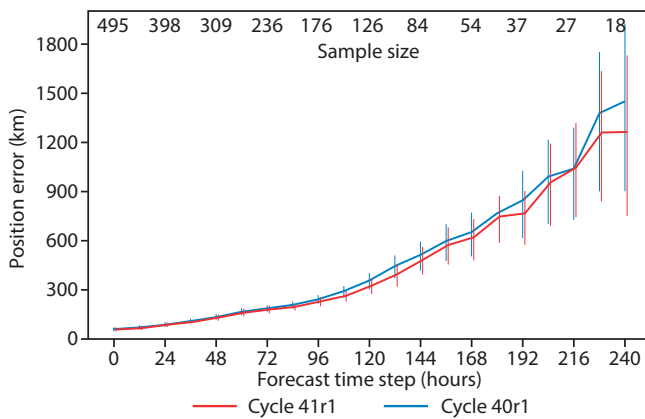
At ECMWF, TC forecasts have been verified routinely for many years. More recently this has been extended to the pre-operational suites. This work is important not only because it provides information about the skill of TC forecasts to users, but also because it gives an indication of the overall quality of the forecast system: an accurate simulation of many different atmospheric processes is needed to be able to correctly predict the evolution of TCs.

Near-real-time reports for TCs issued by the Regional Specialized Meteorological Centres, containing the position and estimated mean sea level pressure at the centre of the storm, are used to verify TC forecasts.

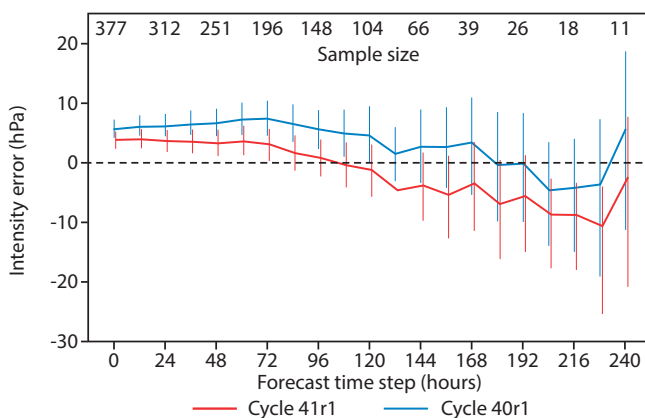
Unfortunately, the verification of TC intensity forecasts does not include most of the basins in the southern hemisphere, with the exception of the South Indian Ocean, because pressure is not routinely reported there.

The results shown here are based on more than 16 months of HRES forecasts (16 km resolution) up to 10 days. To ensure a homogeneous comparison, TC forecasts and observations have to be available in both cycles. This limits the number of forecast/observation pairs, as can be seen by the sharp drop in numbers for longer lead times.

Work is under way to assess how the horizontal resolution upgrade to be implemented in model cycle 41r2 in spring 2016 will affect the accuracy of TC forecasts. Preliminary results indicate that the structural representation of tropical cyclones has improved (better-resolved eye and rain bands), as has the predicted intensity in ensemble forecasts (ENS).



Tropical cyclone position error. The chart shows the TC position forecast mean error as a function of HRES forecast lead time up to 10 days. The bars indicate 90% confidence intervals using the bootstrap method based on 1,000 samples. After 96 hours, position errors are smaller by up to 10% when compared with the previous cycle, although the results are not statistically significant at the 90% level. The reduction in error may be related to significant improvements in predicted mid- and upper-level winds, which act as a steer of TC trajectories, across the tropics in the new cycle.



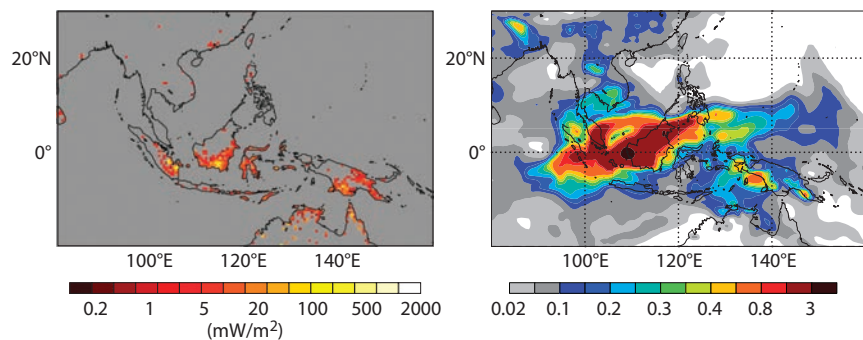
Tropical cyclone intensity error. The chart shows the TC intensity forecast mean error as a function of HRES forecast lead time up to 10 days. The bars indicate 90% confidence intervals using the bootstrap method based on 1,000 samples. The error reduction at analysis time may be related to increased inner-loop resolution in the data assimilation. For longer forecast lead times, there is some indication of degradation (too intense storms) when compared with the previous cycle, but the signal is rather noisy due to small sample sizes.

Monitoring the 2015 Indonesian fires

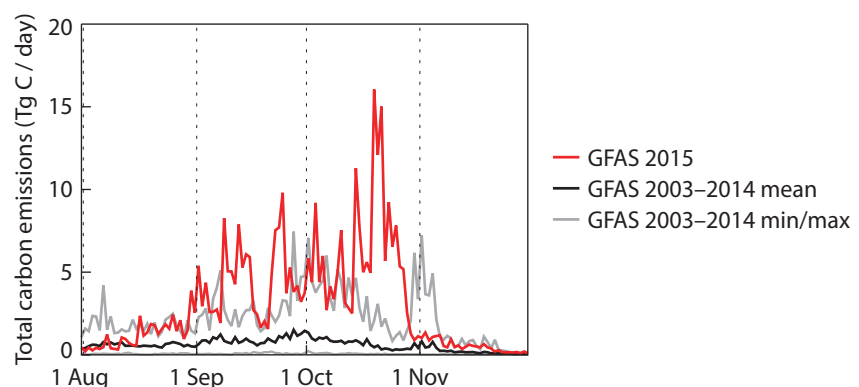
MARK PARRINGTON,
JOHANNES W. KAISER (MPI-C),
SAMUEL REMY (LMD),
MIHA RAZINGER

Large-scale emissions of carbon and smoke from wildfires across Indonesia throughout September and October 2015 have been widely reported by the global media. While fires in this region are commonplace during the dry season, this year they were particularly widespread and persistent due to the dry conditions associated with the current strong El Niño. The strongest fires in the southeastern provinces of Sumatra and the southern provinces of Borneo, originally started for land clearing, burned in peatlands for several weeks, leading to limited visibility and a toxic haze across much of the Maritime Continent (the region between the Indian and Pacific Oceans including Indonesia, the Philippines and the islands of Borneo and New Guinea). For example, in the middle of the burning season, on 23 September, intense fires were observed in many locations with the resultant smoke extending over a wide area around the fires.

As part of the Copernicus Atmosphere Monitoring Service (CAMS), implemented by ECMWF through a delegation agreement with the European Commission, the Global Fire Assimilation System (GFAS) provides near-real-time monitoring of daily global fire locations and emissions. GFAS currently merges fire radiative power (FRP) observations from the two Moderate-resolution Imaging Spectroradiometer (MODIS) instruments on the NASA Terra and Aura Earth observation satellites. Emissions of a variety of smoke constituents, including carbon monoxide (CO), carbon dioxide (CO₂), methane (CH₄), black carbon and organic carbon aerosols, nitrogen oxides (NO_x), and non-methane hydrocarbons (NMHCs), are estimated in GFAS. They are subsequently used as lower boundary conditions for the operational 5-day forecasts and analyses of global atmospheric composition produced by CAMS. The latest version, GFASv1.2, provides a time series that starts in 2003 at a spatial resolution of



Fire radiative power (FRP) and biomass burning aerosol optical depth (AOD). The charts show GFAS-assimilated FRP observations from the MODIS instruments for 23 September 2015 (left) and the smoke contribution to CAMS-assimilated AOD observations at 550 nm from the same instruments across Southeast Asia for the same day (right). FRP values are represented by a logarithmic scale with yellow points being orders of magnitude greater than red points. (Source: CAMS website <http://atmosphere.copernicus.eu/>)



Daily carbon emissions from Indonesia. Time series of total carbon emissions estimated by GFAS from 1 August to 30 November 2015, shown together with average and minimum/maximum emissions for the previous available years (2003–2014).

0.1 degrees, allowing us to compare current emissions with those in previous available years.

Daily carbon emissions for Indonesia approached the maximum daily emissions in the GFASv1.2 record in mid-August and were generally in excess of the previous highest values (mostly associated with the last big El Niño event in 2006) throughout September and October. We estimate total carbon emissions from 1 August to 30 November 2015 to be approximately 0.4 gigatonnes (Gt C), which is equivalent to 1.4 Gt CO₂. This has widely been reported to be in excess of the annual equivalent CO₂ emissions of a number of highly industrialised countries, including the UK and Germany. While GFAS shows that fire emissions in Indonesia in 2015

were considerably higher than in any year since 2003, they were lower than estimated CO₂ emissions during the major El Niño year of 1997, which amounted to approximately 3.5 Gt CO₂. Preliminary assessments attribute about 70% of the 2015 emissions to burning of peat, which has taken centuries and even millennia to form. These emissions are considered to be irreversible, like emissions from fossil fuel burning. The remaining 30% will be extracted again from the atmosphere by vegetation regrowth. The onset of persistent precipitation at the end of October led to a sharp decrease in the number and intensity of the fires. However, based on previous El Niño events, further fires are anticipated for early 2016 and will be monitored by GFAS and CAMS.

Visualising data using ecCharts: a user perspective

ANNA GHELLI, CIHAN SAHIN

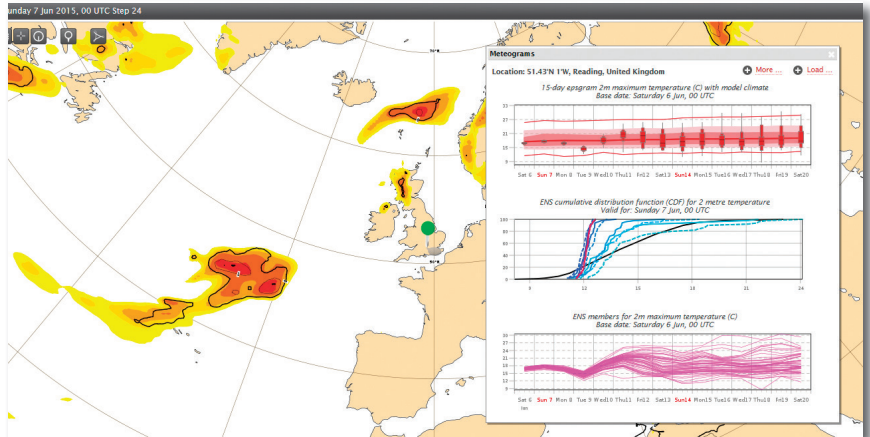
The visual representation of observations and numerical forecasts is paramount to formulating weather forecasts. It can also provide vital background information for decision-making processes. ecCharts, a suite of web browser applications, has been developed at ECMWF to facilitate the interactive visualisation of the Centre’s global numerical weather predictions. It comprises around 170 different products (so-called ecCharts layers) provided every day from model runs at 00 and 12 UTC for both high-resolution and ensemble forecasts (HRES and ENS) up to day 15.

ecCharts goes beyond our standard web charts in that users can use it to create bespoke charts on demand. They can do this themselves as and when they need to, using an easy-to-use web interface.

ecCharts provides:

- An interactive web interface that can be used by users to browse ECMWF forecast products
- A plots-on-demand approach to forecast products so we can provide bespoke/tailored products
- A high-availability web infrastructure so users can rely on our products
- Standard web services to provide computer-to-computer access to web products

ecCharts is a restricted service that is only available to Member and Co-operating State forecasters and



EFI map with meteogram panel. The meteograms provide information on a specific location.

licensed subscribers of ECMWF web products. To enable more national weather services, primarily those from developing countries, to benefit from our full range of web-based charts, we have recently introduced a reduced-fee licence for national weather services that are members of the WMO.

“One of our main tools”

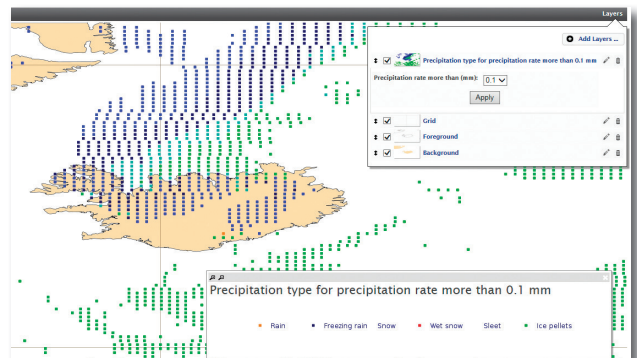
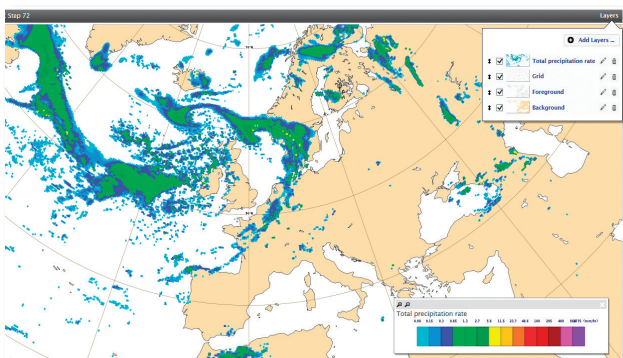
Ivana Petrovic works at the Hydrometeorological Institute of Macedonia, where she leads a team of forecasters. *“We started using ecCharts soon after we discovered it,”* Ivana says. *“We do not have a workstation to visualise ECMWF products and ecCharts was very useful and suited the way we work.”*

As a web application, ecCharts does not require downloading data locally to generate charts. ECMWF model output is pushed to ecCharts clusters as soon as it is available as part of the

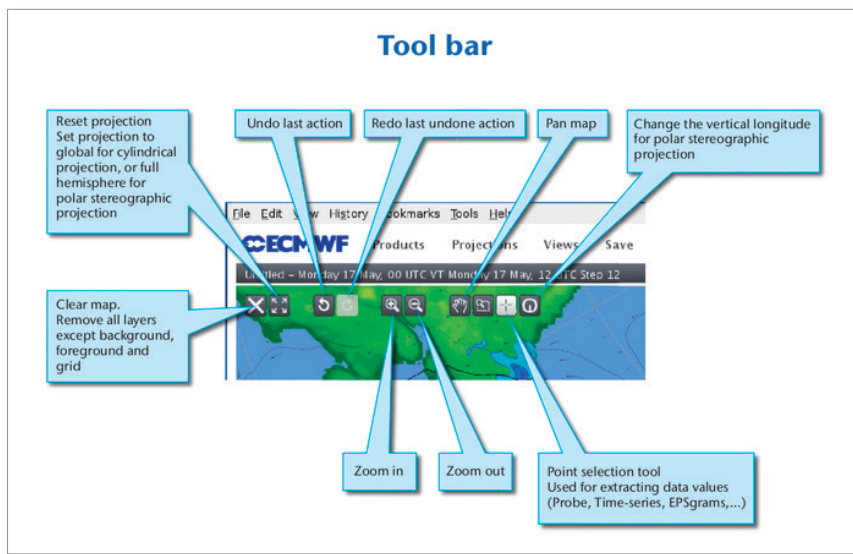
dissemination system. Once the data is available, users can immediately generate charts from the latest forecast run. Different parameters can be overlaid to create custom products. Some layers, such as ENS probabilities, are fully customisable, enabling users to specify their own probability thresholds. Users can create their favourite products and save them for future use.

“The ecCharts user interface is user-friendly and includes a help menu to guide those who approach the web app for the first time,” says Gabriela Bancila, who works as a forecaster in the Romanian National Meteorological Service.

ecCharts allows users to navigate on global meteorological fields either by choosing predefined geographical areas (projections) or by simply panning charts. ecCharts



Precipitation maps. The maps show total precipitation rate (left) and precipitation type (right).



ecCharts tool bar. The ecCharts tool bar gives quick access to a number of functions.

also provides a zooming functionality which allows users to inspect ECMWF data in its native resolution. A dashboard facility is available for users to design and save their frequently used products.

For the Macedonian national weather service, “ecCharts has become one of the main tools used in daily weather forecasting,” Ivana observes.

Added value

ECMWF works in close co-operation with its Member States and Co-operating States to develop and validate products to meet the operational needs for severe weather warnings. These products can be

visualised with ecCharts. “When we expect a period of intense rainfall, we can choose the accumulation period that better represents our risks. Moreover, we can combine parameters such as snow and wind gusts: this is very useful for us in Romania during winter when blizzard episodes are severe,” says Gabriela.

Products are added to ecCharts twice a year based on user requests and new ECMWF model developments. This guarantees that ecCharts evolves continuously.

The ecCharts collection of meteograms enables easy access to point forecasts. The Ensemble

Meteogram is primarily a probabilistic representation of ensemble forecasts and shows the time evolution of the distribution of selected weather parameters for a given location. ecCharts provides various types of meteogram (10-day, 15-day, 15-day with model climate, plumes, 10-day wavegram, individual ENS members, and Extreme Forecast Index (EFI) and cumulative distribution function (CDF) plots) for selected weather parameters. A CDF plot for a quantity provides information on the probability of being above (or below) a set threshold for a specific location. Moreover, plotting CDFs from different forecast lead times verifying at a specified time and location can be used to assess the consistency of the ensemble forecasting system.

“We find it particularly useful to be able to look at point forecasts of ENS parameters and the CDF, which can give us an idea of how severe a particular event is and allows us to provide confident advice to decision-makers and our stakeholders in general,” Ivana says.

For further details on ecCharts, visit <https://software.ecmwf.int/wiki/display/ECCHARTS/Home>

For further details on licensing, visit www.ecmwf.int/en/forecasts/accessing-forecasts/licences-available

Forecasts aid flood action in Peru during El Niño

REBECCA EMERTON,
LIZ STEPHENS & HANNAH
CLOKE (University of Reading),
JUAN BAZO & ERIN
COUGHLAN DE PEREZ (RCCC),
ANA LOPEZ (University of Oxford),
BEATRIZ REVILLA ROMERO
(JBA Consulting),
ERVIN ZSOTER (ECMWF)

Forecast-based Financing is an initiative for disbursing humanitarian funding in advance of a natural disaster, as soon as a forecast threshold is crossed. There are Forecast-based Financing pilot projects in Peru,

Mozambique, Uganda and 12 other countries around the world. Previous strong El Niño events have been known to cause severe flooding in the Piura region of Peru, and with ECMWF forecasts earlier in 2015 indicating the potential for an exceptional El Niño event, flood preparedness in this region became a high priority.

Over the past several months, researchers at the University of Reading, the University of Oxford and ECMWF have been working with the Red Cross / Red Crescent Climate Centre (RCCC), the Peruvian and German Red Cross Societies, and the

Servicio Nacional de Meteorología e Hidrología del Peru (SENAMHI) to analyse the links between El Niño and flooding in Peru, and work towards setting thresholds for action.

Research

The Global Flood Awareness System (GloFAS) has been used to create the first 110-year global reanalysis dataset of river discharge, using the ECMWF ERA-20C atmospheric reanalysis. Using this river discharge data alongside ERA-20C sea-surface temperature (SST) data, the link between El Niño, river discharge and ‘floodiness’ (defined as the percentage



GLoFAS workshop at SENAMHI in Peru. The workshop was delivered by Dr Stephens and Dr Revilla Romero. (Photo: Liz Stephens)



Flood level marks on house in Peru. Discolouring caused by floods in 2012 (upper level) and 2015 (lower level) is visible on this house in Iquitos, Peru. (Photo: Juan Bazo)

of major river cells exceeding a return period threshold) is being investigated. Results show that river discharge is higher, on average, when there is an El Niño. The strength of an El Niño event is determined by the SST anomaly in parts of the tropical Pacific Ocean. River discharge and floodiness in Piura is found to be most highly correlated with SST anomalies in the NINO1+2 region in the far eastern Pacific.

Further research into the changes in atmospheric circulation and precipitation affecting Piura during El Niño events is ongoing and aims to determine the meteorological driver(s) of the most extreme flooding events, such as those in 1982/83 and 1997/98 during exceptionally strong El Niño events.

Verification

The forecasts that will be considered to trigger preventative action include SST anomaly forecasts over the NINO1+2 region two to three months out as well as medium-range total precipitation forecasts for some of the locations where the Red Cross has identified vulnerable populations.

ECMWF’s System 4 (S4) SST forecasts for moderate and strong NINO1+2 events (SST anomalies > 1 and 1.7°C, respectively) have Brier Skill Scores

larger than 0.5 for up to four months out. Reforecasts for the 1982/83 and 1997/98 events show that S4 is able to adequately forecast SST anomalies. For some locations and extreme precipitation events, medium-range forecasts show enough skill to be potentially useful for this application.

Thresholds for action

In August and October 2015, Dr Ana Lopez, Dr Liz Stephens and Professor Hannah Cloke of the Universities of Oxford and Reading spent time in Peru working with SENAMHI and the Peruvian Red Cross.

A key to establishing thresholds for Forecast-based Financing is identifying the best forecasts that are freely available (in this case, to SENAMHI). The ECMWF forecasts, together with forecast products from other sources, will be used to trigger humanitarian actions identified through engagement with Civil Defence Agencies and community groups in the target districts

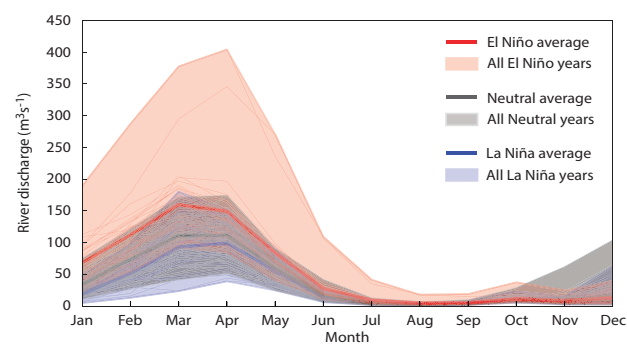
in Peru. The intervention programme is staged, with different actions taken at different lead times. These actions include volunteer training, awareness campaigns, early warning and the purchase and supply of relief items for safe drinking water, health and hygiene and strengthening of houses.

Two workshops have been run at SENAMHI to introduce and provide training for ECMWF forecasts, including GloFAS forecasts. Further training has been provided to initiate collaboration between SENAMHI and GloFAS hydrometeorologists, enabling data sharing for forthcoming model validation.

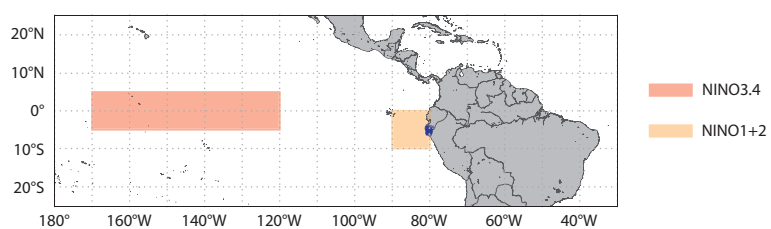
Outlook

Although the probability of an exceptionally strong NINO1+2 event is now low, forecasts are still indicating extreme rainfall in Peru in the coming months. As such, the forecast thresholds to trigger actions with a lead time of two to three months have been met. Actions such as awareness campaigns and volunteer training have begun, and we are waiting to see if actions at shorter lead times will be triggered too. The project team are now also working to establish forecast thresholds for the Amazonian city of Iquitos, which poses different challenges.

This pilot was funded by the German Federal Foreign Office.



River discharge spread. The spread has been determined across all El Niño, neutral and La Niña years, 1901-2010.



NINO1+2 and NINO3.4 regions. These regions can be used to define the strength of an El Niño event based on sea-surface temperature anomalies in the central and far eastern tropical Pacific. The Piura region of Peru is highlighted in dark blue.

Calibrating river discharge forecasts

PAUL SMITH

New calibration methods for the European Flood Awareness System (EFAS) tested at ECMWF have shown the potential to improve forecast skill. ECMWF is the computational centre for EFAS, which is part of the Copernicus Emergency Management Service.

Twice daily the EFAS flood forecasting model is executed using multiple precipitation forecasts, such as those generated by ECMWF,

the German Meteorological Service (DWD) and the COSMO consortium, to provide an ensemble of medium-range flood forecasts across Europe. The EFAS system has highlighted the potential for flooding ahead of a number of events, leading to an improvement in the mitigating actions taken by the authorities responsible for civil protection.

For sites where observed river discharge data is made available in real time by EFAS partners, ECMWF

provides post-processed (also known as calibrated) flood forecasts. The post-processed forecasts are generated by statistically adjusting the ensemble of flood forecasts to offer improved predictions. This allows those receiving the forecasts to compare them with their own warning levels, thus going beyond the climatological warning thresholds used in EFAS.

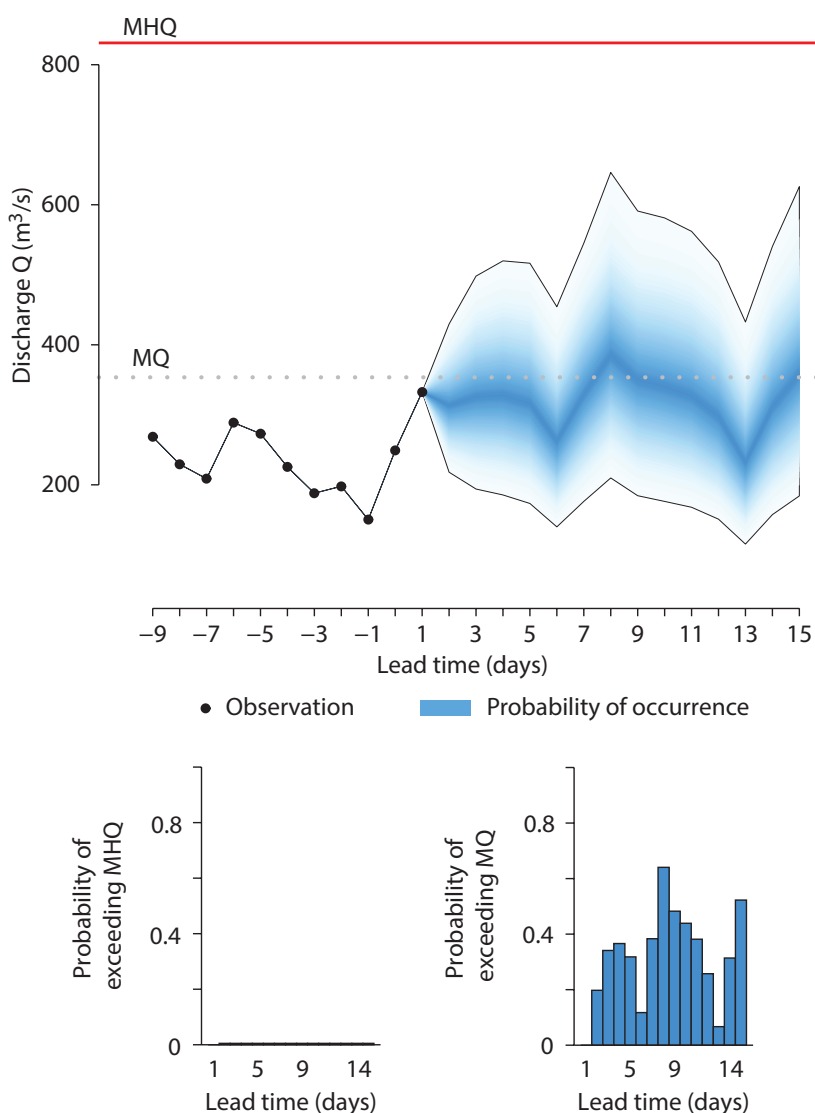
Recent work at ECMWF has focussed on developing an improved post-processing methodology for EFAS. This methodology takes into account the uncertainty arising from the use of predicted meteorological variables to drive the model, and also the inability of the flood forecasting model to represent hydrological processes across the whole spatial domain. This was achieved by developing two statistical models.

The first statistical model describes the joint distribution of the observed data and simulated discharge output, generated by the simulation used to derive the initial conditions of the forecast. This is derived offline using historical data and model simulations (model analysis).

The second statistical model utilises a novel Ensemble Model Order Statistics (EMOS) technique to give a probabilistic forecast of future values of the initial condition simulation, based on the ensemble discharge forecast. This distribution is estimated as part of the forecast generation based on a moving window of data.

Conditioning of the joint distribution in the first statistical model with the available observed and initial condition data along with the EMOS-based forecast distribution leads to the post-processed forecast of discharge values. The resulting forecasts have been shown to have improved forecast skill in a study across 30 key sites in Europe.

Future work will focus on further developing these methods for site-based forecasts. The potential for post-processing to offer improved forecasts across the entire river network will also be investigated.



Example of calibrated discharge forecast. The panels show the prediction of discharge Q (top), the probability of exceeding the mean annual maximum daily discharge (MHQ), which is zero at each forecast lead time in this example (bottom left), and the probability of exceeding the mean daily discharge (MQ) at each forecast lead time (bottom right).

CERA-20C production has started

PATRICK LALOYUX

ECMWF has started the production of a new global 20th-century reanalysis, reconstructing the Earth’s past weather from historical observations. This reanalysis, called CERA-20C, is based on a coupled atmosphere–ocean data assimilation system developed over the last few years in the Research Department. Twentieth-century reanalyses provide a long record of low-frequency climate variability and change using a consistent set of observations. They can serve to provide a longer-term perspective on more recent temperature anomalies. The evolution of the global weather for the period 1901–2010 will be represented by a ten-member ensemble of 3-hourly estimates for ocean, surface and upper-air parameters. The ensemble technique takes into account inevitable uncertainties in the observational

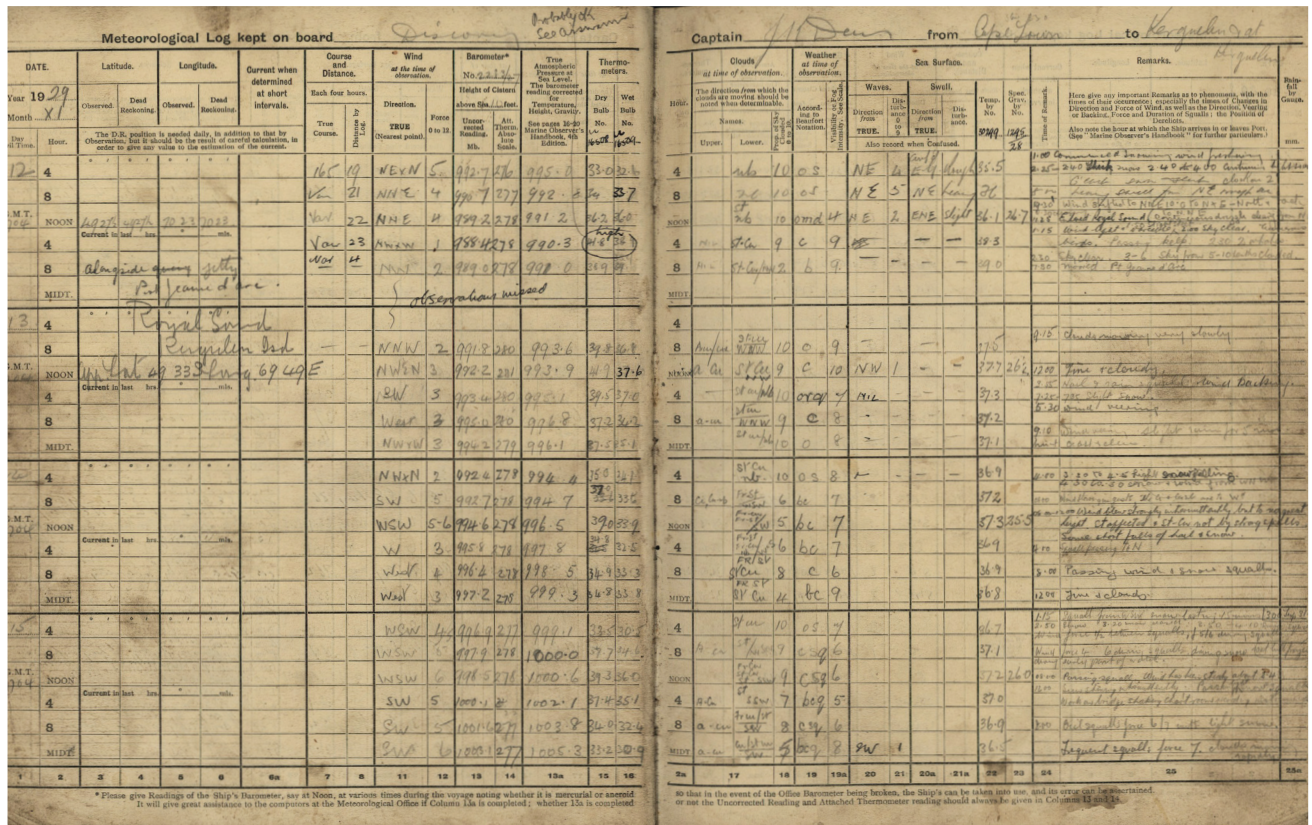
record and the forecast model to provide an indication of the confidence we can have in the data. The CERA-20C reanalysis is part of the EU-funded ERA-CLIM2 project, which builds on the ERA-CLIM project. The latter produced ERA-20C, a first 20th-century reanalysis for the atmosphere (*ECMWF Newsletter No. 141*, p. 9).

From observations to analysis

Climate reanalyses require extended observational datasets with long time series of weather observations. The development and maintenance of these climatic datasets is an expensive undertaking. International initiatives, including the ERA-CLIM and ERA-CLIM2 projects, have rescued and digitised historical daily and sub-daily weather observations. Rigorous quality control processes are used to ensure that the digitised data values correspond to those originally recorded. The availability of these

international datasets is crucial to extend reanalysis activities far back into the past.

Climate reanalyses follow a whitelisting approach to data selection, where observations are used only if they are known to be suitable for climate applications. In the CERA-20C reanalysis, different datasets are used to constrain the atmospheric and ocean components of the Earth system. Mean sea-level pressure and surface marine wind observations have been selected from the ISPDv3.2.6 and ICOADSv2.5 datasets. These surface weather observations are available in large numbers throughout the 20th century. Initially concentrated in the northern hemisphere, the global coverage increases with time. The first 20th-century reanalysis, ERA-20C, showed that a modern data assimilation system and forecasting model are



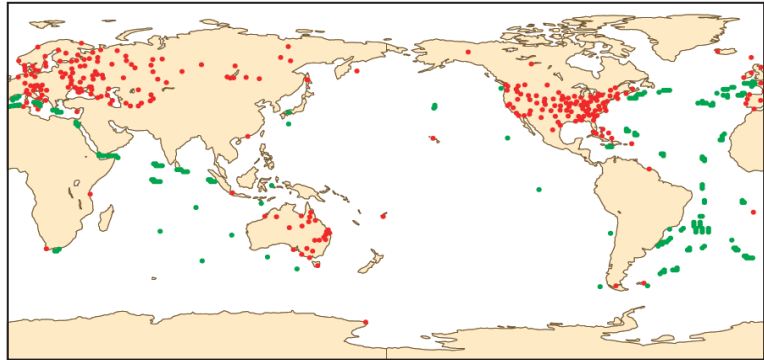
Logbook page from the ship Discovery. During Douglas Mawson’s Antarctic expedition from 1929 to 1931, weather observations such as mean sea-level pressure and surface wind were recorded in the ship’s logbook every 4 hours. These data have been digitised and encoded in international datasets available to climate researchers. (Image: Bureau of Meteorology Special Collections Archive)

well able to reconstruct the large-scale tropospheric circulation from surface weather observations alone. For the ocean component, observed subsurface temperature and salinity profiles have been selected from the EN4 dataset. Finally, the air–sea interface is constrained by an ensemble of different but equally plausible estimates of the sea-surface temperature from the HADISST2 monthly product.

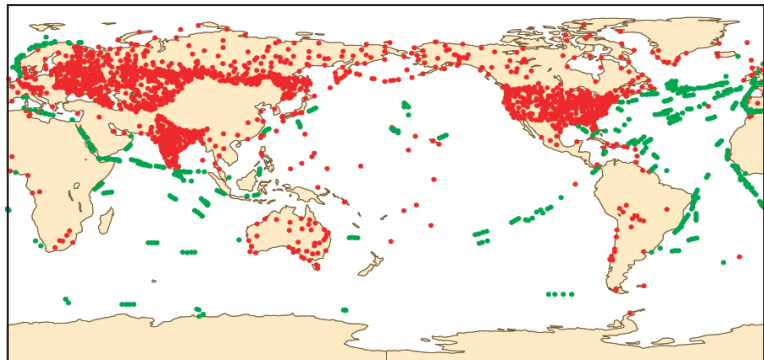
To produce the CERA-20C reanalysis, the selected atmospheric and ocean observations are assimilated simultaneously in the coupled data assimilation system, which computes a consistent atmosphere–ocean analysis. Applying the coupled model constraint in the analysis implies that the assimilation of an ocean observation has an immediate impact on the atmospheric state estimate and, conversely, the assimilation of an atmospheric observation affects the ocean state. The air–sea interface is relaxed towards the HADISST2 monthly product to avoid a rapidly-growing model bias while allowing the simulation of relevant coupled interactions.

The CERA-20C reanalysis takes advantage of the latest developments in ECMWF’s coupled forecast model and data assimilation system. Approximately 1 billion observations from the 20th century will be processed to generate 1 petabyte of reanalysis data. This will contain the evolution of the Earth’s past weather in the form of an ensemble of estimates for all model parameters even if there are no observations for them. Once consolidated, this dataset will be disseminated through a web interface to external users.

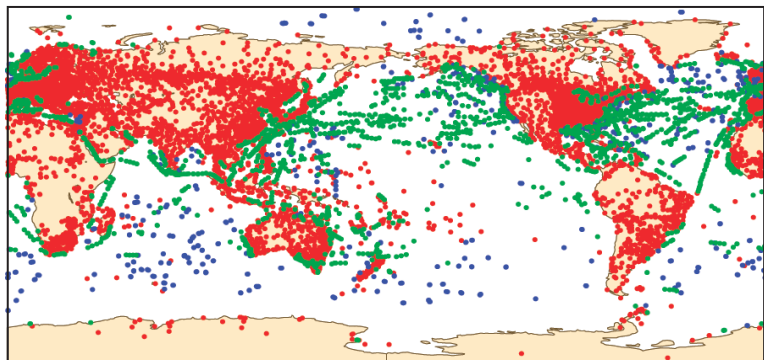
1900



1950



2010



• Land stations • Ships • Buoys

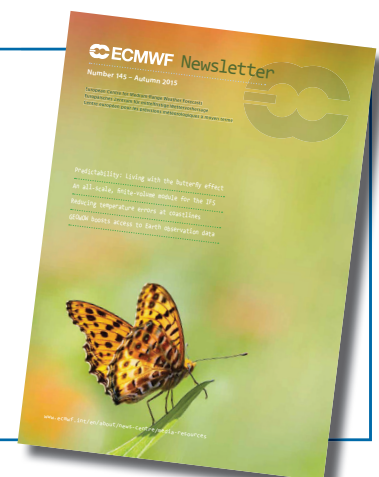
Number of mean sea-level pressure observations per day. The charts show the number of observations in the ISPDv3.2.6 and ICOADSv2.5 datasets used for the CERA-20C reanalysis.

ECMWF NEWSLETTER GOING DIGITAL

As part of our aim to reduce our carbon footprint, we would like to encourage our readers to access the digital version of the ECMWF Newsletter.

Newsletters are already available as PDF documents here: www.ecmwf.int/en/about/news-centre/media-resources, and soon they will be available in fully digital form.

If you would like to be notified when the ECMWF Newsletter is available online, please contact us at newsletter@ecmwf.int and ask to be added to our email alerts list.



Migration to new ECMWF website is complete

**SYLVIE LAMY-THÉPAUT,
ANDREW BRADY,
HELEN SETCHELL**

On 2 December 2015, the migration of content from ECMWF’s old website to its new website was completed. The migration had four main components:

- General content across all areas, including committee documents and user support documentation
- Publications and bibliographic items
- Data and graphical products (charts)
- Dashboard (replacement for ‘Your Room’)

Completing it was the culmination of four years of work. Given its age and its popularity, we knew that decommissioning the old site would be a significant change that would have an impact on users of our services. To reduce any inconvenience, we monitored and audited the old website’s use in order to guide our migration efforts. We are satisfied that, in the end, any disruption to users was kept to a minimum.

On the old site we had over 20,000 pages, 10,000 publications and 140 graphical packages. A lot of redundant and out-of-date content was culled in the interest of a better user experience. On the new site, we now have 1,400 pages and 7,200 publications but the same number of graphical packages. If users have feedback about content

we are very happy to receive it and will endeavour to resolve any issues.

A new searchable eLibrary gives access to all publications on the new site, including ECMWF Newsletters, Technical Memoranda, documentation on the Integrated Forecasting System (IFS) and workshop proceedings.

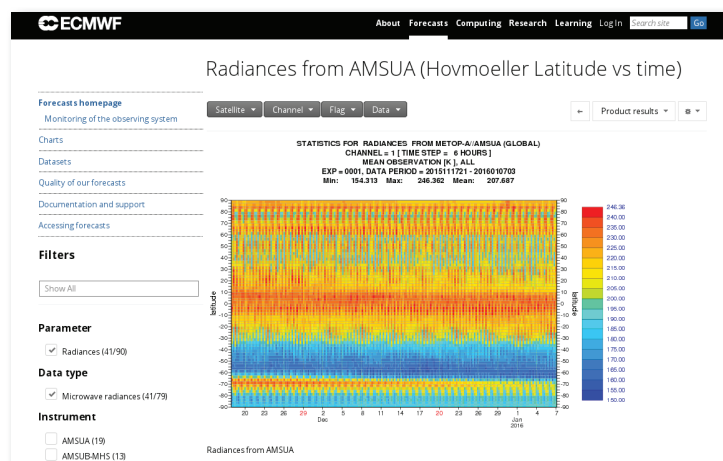
Faceted search

In addition to migrating ECMWF’s graphical products to a new platform, we have aimed to make them easier to discover. To achieve that, it was decided to investigate the use of faceted search. Faceted search has become a popular technique for interactive user interfaces, and many

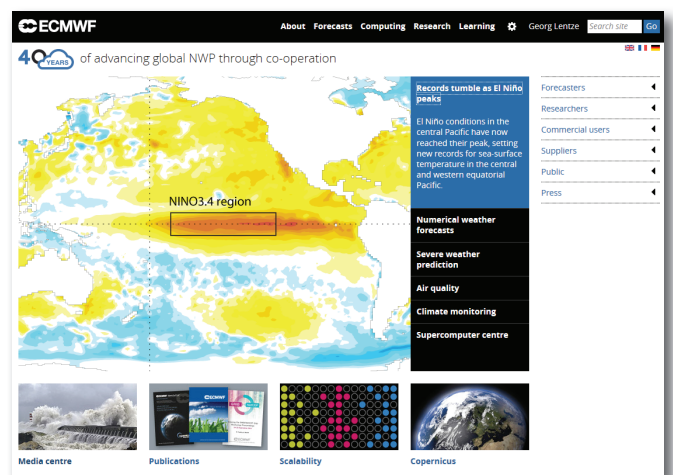
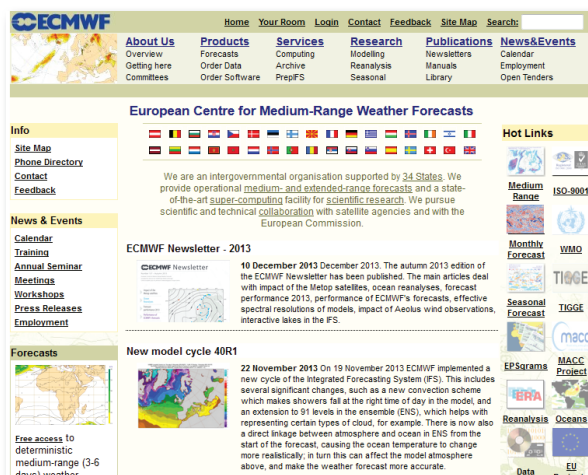
users are becoming familiar with this approach. Its main advantage is that it enables users to find relevant products with minimum effort by filtering for the characteristics they are interested in.

The new ECMWF website faceted search implements an easy-to-use interface. Each of the nearly 700 catalogue products has been carefully reviewed and tagged to ensure that a user’s query will return the right result. This process will be reviewed regularly to take into account user feedback.

Once a product has been discovered, the user needs some easy way to find it quickly in the future. This is the role of the dashboard, which is

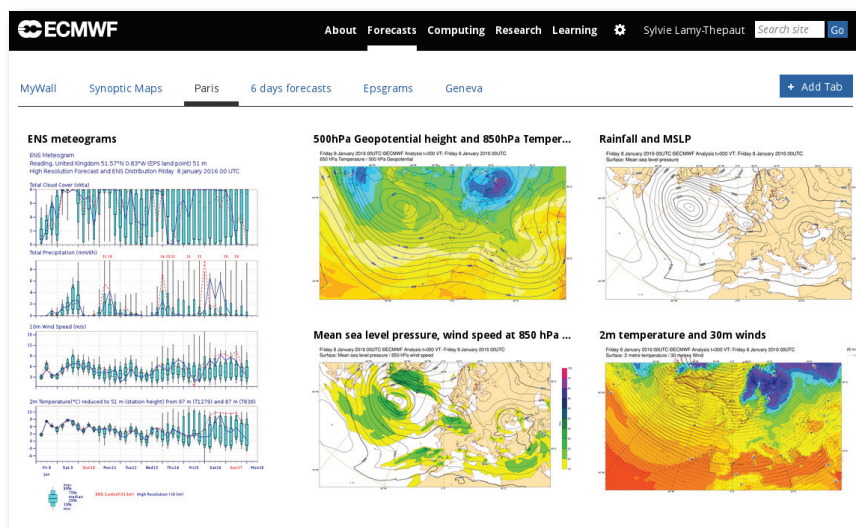


New navigation. The new navigation offers new ways of reaching a product depending on the user’s interests. In this example, users can refine their search according to the instrument they are interested in or a range of other criteria.



Old and new ECMWF website front pages. The old website was retired on 2 December 2015 and the new website is now fully functional.

similar to 'Your room' on the old website. The dashboard enables users to create a fully personalised working environment: once they have found the product they need, they can, with a simple click, save it to their dashboard. Users have full control over the layout and can organise products under tabs. Clicking on a thumbnail gives them quick access to the full-size product in a preview window with basic interaction, such as animation. The dashboard takes advantage of the development of ecCharts, a suite of web browser applications described elsewhere in this Newsletter (pp. 9-10). Looking to the future, we will continue to improve all aspects of our web service. As always, it is your feedback via the 'Contact us' section on the website or directly to calldesk@ecmwf.int that helps us most.



New dashboard. The new dashboard allows users to organise their favourite products.

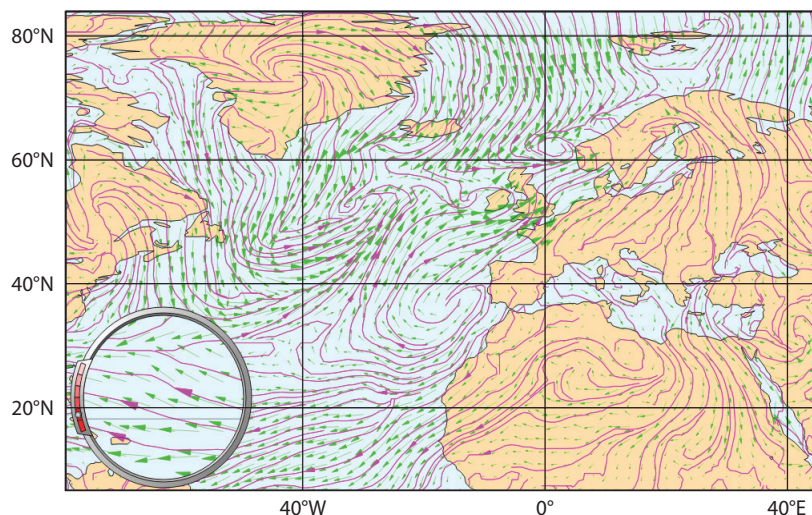
Software updates in preparation for model cycle 41r2

**STEPHAN SIEMEN,
IAIN RUSSELL,
TIAGO QUINTINO,
DANIEL VARELA SANTOALLA**

November and December 2015 saw the first synchronised releases of ECMWF open source software packages for the encoding, decoding, processing and visualisation of meteorological data. Synchronised releases will allow users to migrate more easily to new versions of ECMWF software. Releases will be announced on the Software Support blog at <https://software.ecmwf.int/support>.

The December 2015 release provides full support in all software packages for the new octahedral reduced Gaussian grid which ECMWF will use in its forecasting system from spring 2016.

The implementation of the new grid in the interpolation library Emolib required changes to the code. Tests have shown that interpolation performance has greatly increased and accuracy has improved. This will cause values to change in some cases, but we are confident that these changes are



New features in November release of Magics/Metview. The new Magics/Metview release includes streamlines (shown in purple) in wind charts and the possibility to clip wind arrows at the chart's border for cleaner-looking maps.

correct. Therefore, we ask users to test and evaluate Emolib 4.3 carefully before using it operationally. All these packages use the same build system based on CMake, simplifying and harmonizing the installation experience. For the first time a software bundle for Metview is offered. It comes in the form of a 'tarball' containing the source code

for Metview and all associated software packages from ECMWF. This allows users who want to install Metview to just download one package and configure and build Metview and its dependencies in one go.

We would welcome any feedback on these releases. Please email it to Software.Support@ecmwf.int.

Reducing systematic errors in cold-air outbreaks

RICHARD FORBES, ALAN GEER,
KATRIN LONITZ, MAIKE AHLGRIMM

Models and observations both have uncertainties. Characterising and representing uncertainty and its growth in time is a significant activity at ECMWF with the development of ensemble forecasts (ENS) and more recently the Ensemble of Data Assimilations (EDA). At the same time, an ongoing challenge of research and development is to reduce uncertainties in both the initial state and the forecast model through improvements in the use of observations, data assimilation methodologies and the fidelity of the model dynamics and physics.

Comparing model forecasts with observations on medium-range to seasonal timescales can highlight systematic errors, but non-linear interactions and feedbacks make it difficult to attribute the errors to a particular source. Using short-range forecasts in the data assimilation system, on the other hand, means the model state is reasonably close to reality, and systematic departures of these forecasts from the observations are more easily assessed. Such assessments may even make it possible to identify regime- (or flow-) dependent systematic errors and to attribute these errors to specific physical processes.

In this article, we describe how this approach has enabled us to identify supercooled liquid water cloud in convective cold-air outbreaks as the source of regime-dependent systematic model errors in simulated microwave radiance and shortwave radiation. A proposed solution reduces the model errors at all forecast lead times. This is seen in reduced bias against assimilated microwave observations and reduced shortwave radiation error.

All-sky microwave radiance errors

The first part of the tale is about diagnosing systematic model errors using the data assimilation scheme in ECMWF's Integrated Forecasting System (IFS). Data assimilation combines the model with observations in an optimum analysis of the atmospheric state that is better than either the model or observations on their own. It is designed to minimise random errors, but there are also many systematic differences between models and observations. In practice, such differences are removed by the observational bias correction process, but if the model bias is too large it is better not to assimilate the affected observations. These systematic differences deserve careful study: whether they are associated with the model, the observation operator, or the observations, they indicate a scientific problem that needs fixing at source.

Microwave imager radiances in clear, cloudy and precipitating conditions (also known as all-sky conditions) have been assimilated operationally into the IFS since 2009 (Bauer *et al.*, 2010). Typical instruments like the Special Sensor Microwave Imager/Sounder (SSM/I/S, see Box A)

Satellite observations

A

Microwave radiometer SSM/I/S

The Special Sensor Microwave Imager/Sounder (SSM/I/S) is a passive microwave radiometer on board a series of Defense Meteorological Satellite Program (DMSP) near-polar-orbiting satellites. The SSM/I/S instrument measures microwave radiance at 24 discrete frequencies from 19 to 183 GHz with different sensitivities to atmospheric temperature, water vapour, rain, cloud liquid water, and at higher frequencies also cloud ice and frozen particles. The 37 and 92 GHz channels are particularly sensitive to vertically integrated cloud liquid water.

CERES shortwave and longwave radiation

The Clouds and the Earth's Radiant Energy System (CERES) instrument passively measures both the solar-reflected and Earth-emitted radiation from the atmosphere. There are instruments on board a number of polar-orbiting satellites (Aqua, Terra, NPP) providing global coverage in a 24-hour period.

MODIS visible image

The Moderate Resolution Imaging Spectroradiometer (MODIS) passively measures electromagnetic radiation across a wide spectrum and is on board both the NASA Terra and Aqua polar-orbiting satellites, completely observing the whole globe in 1 to 2 days. The true-colour image combines the red (670 nm), green (565 nm) and blue (479 nm) channels to create a view similar to that which would be seen by the human eye.

CloudSat and CALIPSO

CloudSat and CALIPSO are near-polar-orbiting satellites carrying a 94 GHz radar and a multi-frequency (532/1064 nm) lidar, respectively. Both instruments are active in the sense that they emit a signal and measure the backscatter from the atmosphere, clouds and precipitation. The lidar signal is strongly attenuated by small cloud droplets, enabling the identification of liquid water layers near cloud top at any temperature.

measure a range of frequencies with strong sensitivities to atmospheric water vapour, rain, snow and liquid water cloud. Differences between the observations and a short-range forecast (0–12 hours) within each assimilation cycle are called first-guess departures. A forward operator calculates the predicted microwave radiance brightness temperatures from the model geophysical fields to compare directly with the observations. The first-guess departures can be a valuable source of information on systematic model errors, or 'biases'. However, because they are expressed in radiance terms and because the radiances are affected by a range of atmospheric and surface parameters, it can sometimes be difficult to attribute these departures to a particular cause.

Figure 1a shows the annual mean first-guess departures for the SSMI/S 92 GHz microwave radiance brightness temperature for the operational IFS high-resolution model (HRES) for 2014–2015 over the oceans. Significant positive differences are apparent towards the polar side of the extra-tropical storm track in the southern and northern hemispheres as well as in the maritime stratocumulus regions off the coast of South America and Africa, and to a smaller extent along the inter-tropical convergence zone (ITCZ) over the Pacific Ocean.

The extra-tropical storm track brightness temperature departures have been a long-standing difficulty when assimilating the microwave imagers in all-sky conditions. Since systematic first-guess departures can degrade the analysis, the observations involved have had to be screened out. Several years ago significant first-guess departures were found to be associated with cold dry air moving equatorward behind cold fronts in the winter hemisphere (Geer & Bauer, 2010). These are regions where convection is active due to the instability produced by cold air flowing over the warmer ocean and where positive departures for certain microwave frequency brightness temperatures were often 5 to 10 K. Due to the low water vapour in these cold air masses in the model and the insensitivity of these microwave frequencies to cloud ice particles, a lack of cloud liquid water in the model is the most obvious explanation for the problem. Although targeted screening of the observations in these regions can avoid degrading the analysis (Lonitz & Geer, 2015), a more desirable approach is to improve the model physics to reduce the first-guess departures and be able to assimilate these observations.

Shortwave radiation errors

The second part of this tale is the long-standing systematic error in the global shortwave radiation field. The top-of-atmosphere radiation is a direct well-observed quantity globally available from polar-orbiting and geostationary satellites and is an important metric for evaluating models across a wide range of space and timescales. In particular, the reflected shortwave radiation is significantly affected by the surface albedo and by cloud. Shortwave radiation errors in the IFS are routinely evaluated at ECMWF and show an improvement over the last decade due to a better representation of cloud as well as surface albedo. However, there are certain long-standing systematic errors in the shortwave radiation that continue to be present in the IFS at all forecast time ranges and model resolutions, suggesting deficiencies in the representation of cloud-related physical processes.

Figure 1b shows the annual mean top-of-atmosphere net shortwave radiation bias over the oceans in HRES for 2014–2015. The largest signal is from the subtropical marine stratocumulus regions in the eastern part of major oceanic gyres. However, there is also a significant positive shortwave radiation bias centred around $\pm 60^\circ$ latitude in the northern and southern hemisphere storm tracks over the North Atlantic, North Pacific and Southern Ocean, similar to the pattern of microwave radiance bias seen in Figure 1a. The storm-track errors are the focus of this article, but both the

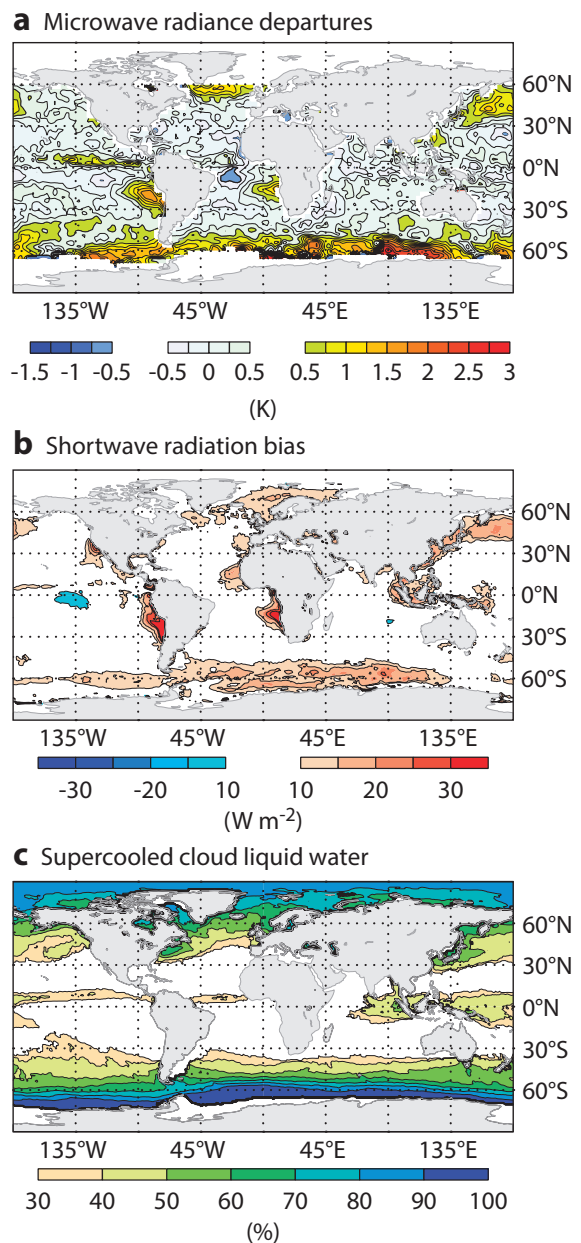


Figure 1 Annual mean from the operational IFS HRES (May 2014 to April 2015) for (a) SSMI/S microwave 92 GHz brightness temperature first-guess departures in the data assimilation scheme (model minus observations), (b) 24-hour forecast top-of-atmosphere net shortwave radiation difference from CERES satellite observations (model minus observations) and (c) percentage of the total vertically integrated cloud liquid water that is supercooled.

maritime stratocumulus and higher-latitude signals are consistent with either too little cloud cover, too little cloud water path, or incorrect optical properties, leading to not enough reflection back to space and too much radiation reaching the surface. Similar systematic errors are present at all resolutions of the IFS and at all forecast lead times out to seasonal timescales (as will be shown later). In addition, similar errors can be seen in many other numerical weather prediction (NWP) and climate models, so the problems are not specific to the IFS.

Supercooled liquid water cloud

We next explore the potential link between the systematic model errors seen in the shortwave radiation and the suggestion, based on microwave radiance observations, that in some situations the vertically integrated cloud liquid water in the model is too low. At the latitudes of the northern and southern hemisphere storm tracks, the temperature of the cloud top is often below 0°C. Figure 1c shows the global annual mean distribution of the percentage of the vertically integrated cloud liquid water content that is supercooled (i.e. the proportion of cloud liquid water at temperatures colder than 0°C). The data is again from the operational HRES for 2014–2015. Supercooled liquid water (SLW) has a significant presence in the mid-latitude storm tracks in both hemispheres, with 50–100% of cloud liquid being supercooled in the region of the shortwave radiation and SSMI/S brightness temperature biases. There is a seasonal shift north and south corresponding to the seasonal cycle (not shown). Although this is a model estimate, these regions with significant supercooled water in the IFS are consistent with the spatial distribution of supercooled liquid water occurrence observed from satellite lidar (*Hu et al., 2010*), which is particularly sensitive to small liquid water drops at cloud top.

Based on previous studies, we also know that supercooled liquid water has a significant impact on the reflection of shortwave radiation, particularly when it is present at cloud top. The microwave radiance assimilation suggests a lack of cloud liquid water in the areas of convective cold-air outbreak, and these regions are also where the cloud is mostly colder than 0°C. The overall hypothesis is therefore that it is a lack of supercooled liquid water at cloud top in the convective cells associated with cold-air outbreaks that is the cause of the errors in both microwave radiances and the shortwave radiation.

A regime-dependent systematic error

We focus on one particular day during August 2013 in the southern hemisphere storm track to illustrate the relationship between different variables and diagnose the specific model error (note that we could have chosen any

number of days which show similar features).

Figure 2a shows the MODIS visible image (Box A) for a region to the west of South America between 60°S and 30°S (70°W–130°W) valid for around 12 UTC on 24 August 2013. This region is characterised by a deep frontal cloud band in the eastern half of the domain, bending towards the west in the northern part of the domain. In the south-western quadrant there is a region of convective cells, where cold air is flowing equatorward from the Antarctic ice sheet over the warmer water of the Southern Ocean behind the front. The warmer ocean provides the instability to produce convection over a large region in what is often known as a cold-air outbreak.

Figure 2b shows the total cloud cover from an IFS 12-hour forecast (reference forecast, REF) valid at approximately the same time as the MODIS image. The short-range model forecast is close to the analysis and accurately captures the locations and variations of the different cloud regimes, from the overcast frontal cloud to the broken cloud cover associated with the convective cold-air outbreak behind the front.

Figure 3a shows the corresponding vertically integrated total liquid water path (LWP) from REF, highlighting the high liquid water content associated with the frontal band and smaller LWP associated with warm-phase low-level cloud in the north of the domain. However, there is an almost complete absence of liquid water in the region of cold convection, where the cloud in the model is present but essentially all ice.

The CloudSat and CALIPSO satellites with radar and lidar instruments passed across the region of cold-air convection later that same day. A vertical cross section showing cloud phase obtained from radar/lidar data (Box A) from 70°S to 30°S is shown in Figure 4a. The flow is from the south (left-hand side of the figure) and shows the growth of the mixed-phase cloud-topped boundary layer due to increasing surface heat fluxes from the warmer ocean below. There is a transition to convection at about 60°S. The 0°C isotherm from the model shows that all the liquid near the top of the boundary layer cloud to the south of 40°S is supercooled. Note the presence of supercooled water

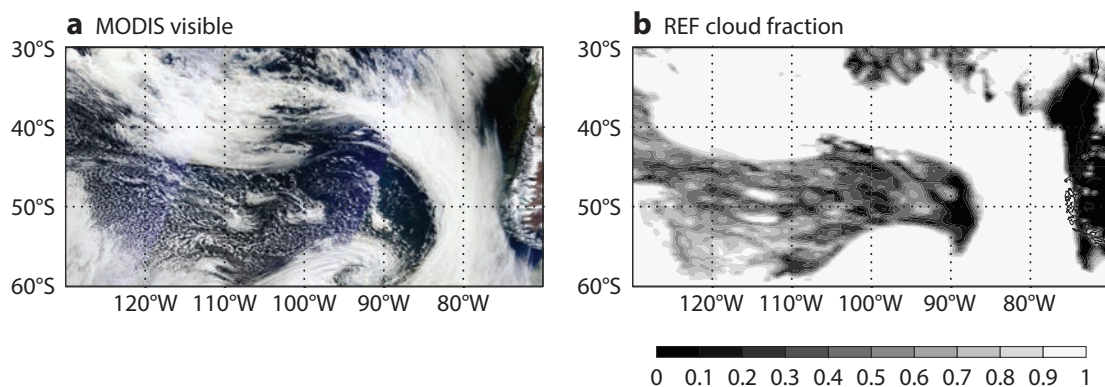


Figure 2 (a) MODIS visible image for approximately 12 UTC on 24 August 2013 and (b) 12-hour forecast of cloud fraction from the reference IFS (REF) valid at 12 UTC.

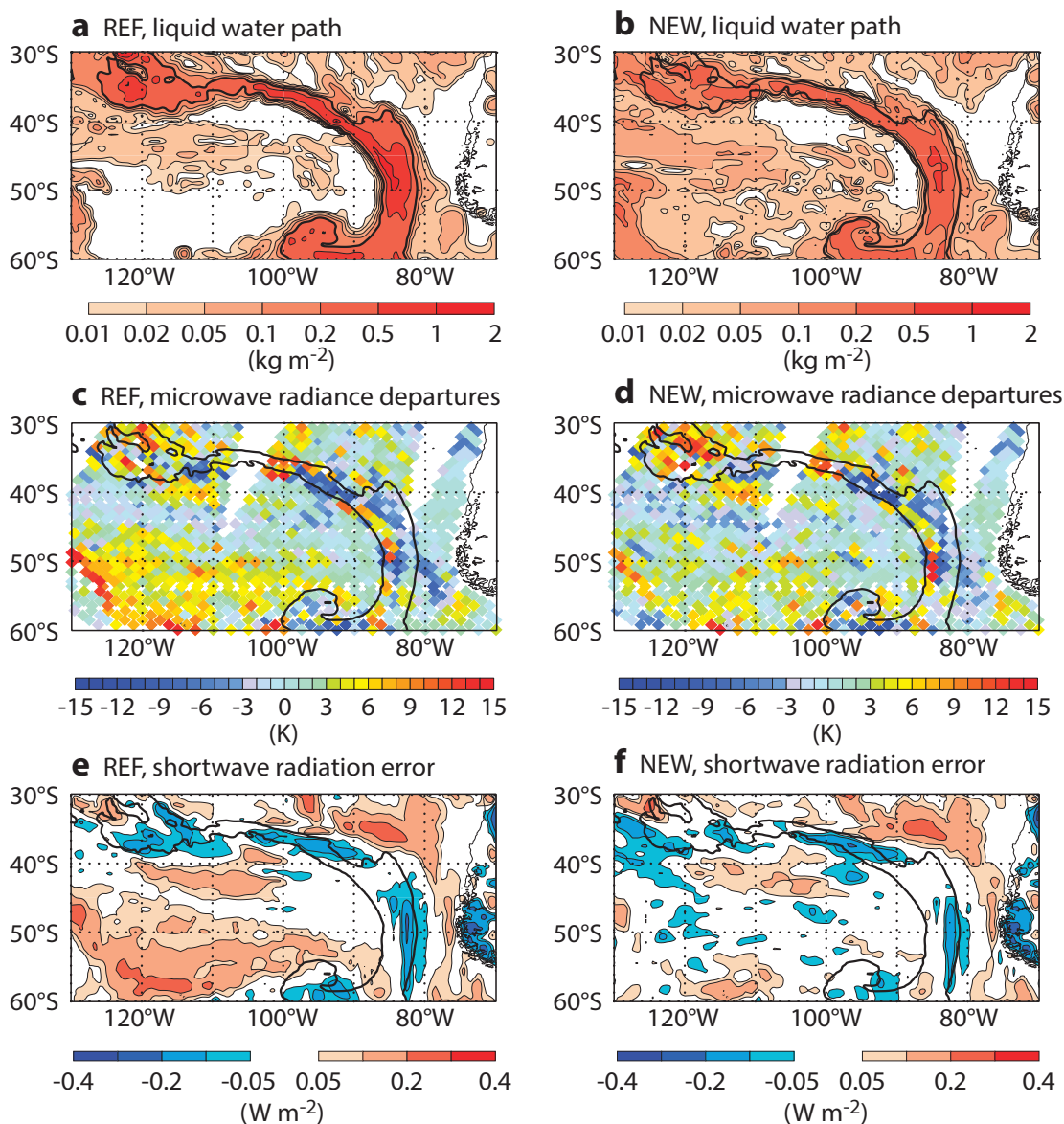


Figure 3 Model fields for 24 August 2013 for the reference IFS (REF; left-hand column) and the IFS with modified convective supercooled liquid water detrainment (NEW; right-hand column) showing (a, b) total liquid water path at 12 UTC from a 12-hour forecast, (c, d) SSMI/S 92 GHz brightness temperature first guess departure in the 12 UTC analysis and (e, f) 24-hour forecast averaged net top-of-atmosphere shortwave radiation difference from observations (IFS – CERES).

in the cold-air convection at cloud top between 60°S and 50°S with temperatures below -20°C . Note also that the radar/lidar combination will only be able to observe liquid water close to cloud top so there is more uncertainty in the cloud phase lower in the cloud. Figure 4b shows the cloud phase for the IFS equivalent to the observed cross section. The cloud phase is calculated by simulating the satellite track and radar/lidar signals in the model and is therefore a comparable product to the observations. The lack of any significant supercooled water is evident between about 60°S and 45°S.

The first-guess departure for SSMI/S 92 GHz microwave radiance brightness temperature in the analysis valid for the same date and time at 12 UTC is shown in Figure 3c. The observations suggest this lack of supercooled liquid in

the convective region is a real deficiency of the model, with positive departures of 5–10 K. There are also large brightness temperature departures associated with the frontal cloud band, but these are more randomly distributed with adjacent positive and negative values associated with slight displacements of the front and small-scale uncertainties.

The final piece to complete the picture is the shortwave radiation bias, which is shown in Figure 3e. The figure shows the IFS shortwave radiation bias over the 24-hour period centred on 12 UTC on the same day, using observations from the daily average CERES dataset compiled from multiple satellite sources (Box A). These observations show there is too little radiation being reflected back to space in the cold-convective region, where there is also negligible supercooled cloud water in the model.

This same pattern of correlated errors in supercooled liquid water and shortwave radiation is repeated over and over in the convective cold-air outbreak regime in both the southern and northern hemispheric storm track, and it can explain the mean errors in the shortwave radiation in the IFS. The reason the error is dominant in the southern hemisphere is due to the high occurrence of the cold-air convection regime over the Southern Ocean. Modifying the physical process parametrizations that affect cloud phase should therefore lead to a reduction of the error in both hemispheres.

Reducing the error

Supercooled liquid water cloud is a challenge to represent in large-scale models because its presence is dependent on a balance of many processes. These include small-scale turbulent production of water saturation; ice nucleation and subsequent ice particle growth through water droplet evaporation (the Wegener-Bergeron-Findeisen process); and riming (falling ice particles collecting and freezing supercooled water droplets). There are therefore many uncertainties in parametrizing these processes in atmospheric models for both stratiform and convective cloud.

Before the end of 2010, the IFS represented mixed-phase cloud with a fixed global diagnostic temperature-dependent function. This meant that cloud was considered to be all liquid for temperatures warmer than 0°C, all ice for temperatures colder than –23°C, and a decreasing proportion of supercooled liquid water in between. A similar diagnostic approach to partitioning cloud phase has been common in global models with relatively simplified microphysics parametrization and is designed to be a first approximation to the global average occurrence of supercooled liquid water. However, in reality condensate in a cloud at a particular location and given temperature (say –10°C) can be all supercooled liquid or all ice depending on the history of the cloud and its environment.

In November 2010, a new cloud scheme was introduced in the IFS with separate predicted variables for cloud ice and cloud liquid and a more physical parametrization of mixed-phase microphysical processes (Forbes & Tompkins, 2011), allowing an improved representation of supercooled liquid water for stratiform cloud (Forbes & Ahlgrimm, 2014). However, the convection parametrization retained the fixed diagnostic temperature-dependent function, with all liquid at 0°C changing to all ice at –23°C. It is the convective mixed phase that is the relevant process in this study.

As seen in the cross section in Figure 4a, the cloud top in the convective cold-air outbreaks, identified as the problem regime, can often be colder than –20°C. Whereas supercooled water is observed at cloud top in these regions, the IFS convective parametrization by definition cannot produce much supercooled liquid at these cold temperatures. Modifying the diagnostic function to produce supercooled water at colder temperatures is one straightforward solution, but this also affects the deeper tropical convection, resulting in increased radiation biases due to an overprediction of supercooled liquid in the

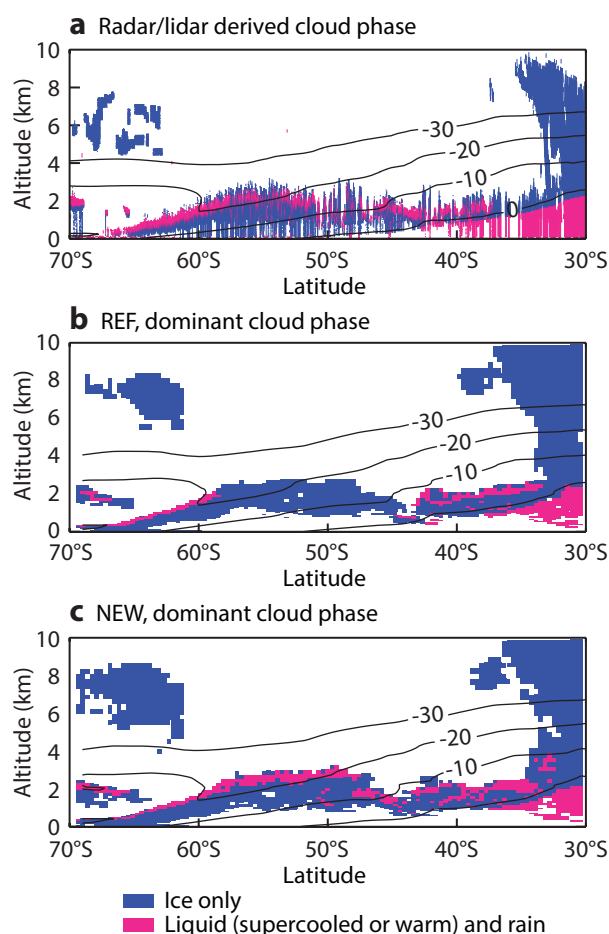


Figure 4 Vertical cross section of dominant cloud phase at about 2230 UTC on 24 August 2013 from latitude 70°S to 30°S close to longitude 120°W through the region of cold-air convection for (a) satellite radar/lidar-derived cloud phase from the DARDAR combined CloudSat/CALIPSO product, (b) model-simulated cloud phase from the reference IFS 12-hour forecast (REF) and (c) from the IFS forecast with modified convective supercooled liquid water detrainment (NEW). Temperature contours are shown every 10°C from 0° to –30°C.

tropics. In fact the unique property of cloud tops at these temperatures is that there is a source of supercooled liquid, which is detrained from the strong convective updraughts, while the sink is primarily through the process of ice nucleation leading to slow glaciation over time. In deeper convection in the tropics there may already be significant frozen particles (snow or graupel) falling through the liquid, which acts to freeze or evaporate the drops, leading to less supercooled liquid water for the same temperature. The convection scheme therefore needs to capture this additional physics in order to differentiate between the deeper convective cloud with less supercooled liquid and the mid-level convective cloud with supercooled liquid present at cloud top.

To test the hypothesis, we performed a series of forecast experiments (NEW), equivalent to the reference (REF) but with modifications so that the convection produces all

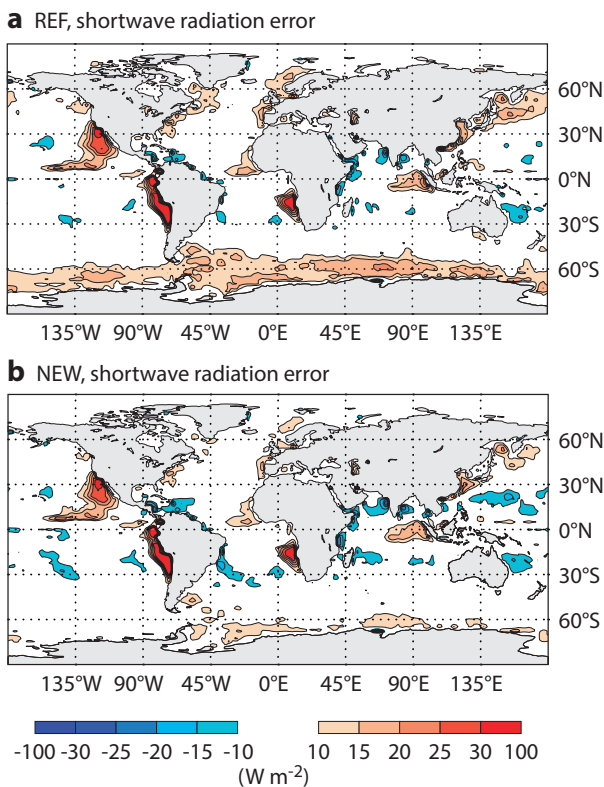


Figure 5 Difference between annual (2000–2001) mean top-of-atmosphere net shortwave radiation over the ocean in a 1-year IFS simulation at the resolution of the seasonal forecasting system (TL255) and in CERES satellite observations for (a) the reference IFS (REF) and (b) the IFS with the modified convective supercooled liquid water detrainment (NEW). The systematic error in the North Atlantic, North Pacific and Southern Ocean storm tracks is significantly reduced.

liquid condensate if the cloud top is below 600 hPa. For convective cloud tops higher than this the existing 0 to -23°C diagnostic phase function is used. Figure 3b,d,f shows the local impact in the Southern Ocean case study for liquid water path, microwave brightness temperature first guess departures and the shortwave radiation error. Liquid water is now present in the convective region where there were negligible amounts before; the 92 GHz first-guess departures are significantly reduced in the cold-air convection; and the shortwave radiation error is almost completely removed. The equivalent cross section to compare with the CloudSat/CALIPSO track across the convective region (Figure 4c) now shows the presence of supercooled liquid water in the cloud across the convective region and particularly at cloud top, in better agreement with the observed data.

The change also reduces the global time-mean bias in the shortwave radiation seen in Figure 1b. Figure 5a shows the annual mean top-of-atmosphere net shortwave radiation bias for a 1-year simulation of the IFS at the resolution of the seasonal prediction system (TL255, 80 km grid resolution). Although not exactly the same, the bias in this 1-year forecast at low resolution is remarkably similar to the 24-hour forecast bias at the operational 16 km grid resolution (Figure

1b), showing the robustness of the shortwave radiation systematic errors across scales. Figure 5b shows the impact of the modifications to the parametrization of convective supercooled liquid water. There is indeed a marked reduction in the shortwave bias, not only across the Southern Ocean, but also in the poleward storm track regions of the North Atlantic and North Pacific Oceans. Early results suggest a similar improvement for the higher-resolution model.

Summary and outlook

This article describes an example of using the data assimilation system to help to identify a regime-dependent systematic error in the model that can be linked to a specific parametrized process. An evaluation of the microwave radiance brightness temperature first-guess departures, combined with shortwave radiation and radar/lidar data from satellites, pointed to a lack of supercooled liquid water in the modelling of convective cold-air outbreaks in both hemisphere storm tracks. It is this combination of data sources that made it possible to identify the problem in the model and, importantly, to provide quantifiable information on the magnitude of the error. A solution that increases the detrained supercooled liquid water for convective updraughts with mid-level (below 600 hPa) cloud tops, which can be colder than -20°C , improves the first-guess fit to microwave radiances in the data assimilation scheme and the model impact of cloud on shortwave radiation. The long-standing shortwave radiation bias over the Southern Ocean, North Atlantic and North Pacific, seen at all IFS model resolutions and timescales from a few hours to seasonal timescales, is significantly reduced.

More work is required to assess the seasonal cycle of the errors and to implement a more physically based solution in the operational model. It will be important to assess downstream impacts of the reduction in these systematic errors, particularly on the sea-surface temperature in the coupled atmosphere–ocean configurations of the IFS.

FURTHER READING

Bauer, P., A. J. Geer, P. Lopez & D. Salmond, 2010: Direct 4D-Var assimilation of all-sky radiances. Part I: Implementation. *Q.J.R. Meteorol. Soc.*, **136**, 1868–1885.

Forbes, R. M. & M. Ahlgrim, 2014: On the representation of high-latitude boundary layer mixed-phase cloud in the ECMWF global model. *Mon. Wea. Rev.*, **142**, 3425–3445.

Forbes, R. & A. Tompkins, 2011: An improved representation of cloud and precipitation. *ECMWF Newsletter No. 129*, 13–18.

Geer, A. J. & P. Bauer, 2010: Enhanced use of all-sky microwave observations sensitive to water vapour, cloud and precipitation, *ECMWF Technical Memorandum No. 620*.

Hu, Y., S. Rodier, K.-M. Xu, W. Sun, J. Huang, B. Lin, P. Zhai & D. Josset, 2010: Occurrence, liquid water content and fraction of supercooled water clouds from combined CALIOP/IIR/MODIS measurements. *J. Geophys. Res.*, **115** (D4), D00H34.

Lonitz, K. & A. Geer, 2015: New screening of cold-air outbreak regions used in 4D-Var all-sky assimilation, *EUMETSAT/ECMWF Fellowship Programme Research Reports No. 35*.

A new grid for the IFS

SYLVIE MALARDEL, NILS WEDI, WILLEM DECONINCK,
MICHAEL DIAMANTAKIS, CHRISTIAN KÜHNLEIN,
GEORGE MOZDZYNSKI, MATS HAMRUD,
PIOTR SMOLARKIEWICZ

ECMWF will implement a resolution upgrade for high-resolution forecasts (HRES) and ensemble forecasts (ENS) in spring 2016. HRES will then be run on a grid with a grid-point distance between neighbouring points of approximately 9 km instead of 16 km in the current configuration.

In the Integrated Forecasting System (IFS), many calculations are not carried out in grid-point space but in 'spectral space', where meteorological fields are represented by a sum of wave functions called spherical harmonics. As part of the resolution upgrade, ECMWF will move from a 'linear' to a 'cubic' grid by increasing the number of grid points used to represent each wavelength while keeping the number of spherical harmonics constant.

At the same time, it will use an octahedron-based method to reduce the number of grid points towards the poles. The resulting new 'cubic-octahedral' grid brings significant benefits in terms of computational efficiency and effective resolution.

From linear to cubic

The spectral transform method (Box A) has been applied successfully at ECMWF for more than 30 years, with the first spectral model introduced into operations at ECMWF in April 1983. The spectral transform method was introduced to numerical weather prediction (NWP) following the work of *Eliassen et al.* (1970) and *Orszag* (1970), who achieved high efficiency by partitioning the computations between a grid-point and a spectral representation at every time step.

In a spectral transform model such as the IFS, the horizontal wind, the temperature and the surface pressure have a discrete representation in two different spaces. In grid-point space, the representation of the fields is intuitive: each field is known by its value at each point of the model grid. The field discretisation in spectral space is more abstract. The idea is to represent the fields by a sum of analytical functions, the spherical harmonics, such that the sum of the spherical harmonics closely matches the field at each grid point. Each field is then known by the set of coefficients associated with the spherical harmonics in the sum (Box A). Each spherical harmonic has a characteristic horizontal wavelength, which is given by the value of its total wavenumber n . The wavenumber n indicates how many of the characteristic horizontal wavelengths are needed

Global spectral transforms

A

In the IFS, the horizontal wind, the virtual temperature and the surface pressure are transformed to spectral space and back to grid-point space at every time step. All the water variables and the passive tracers, e.g. specific humidity and prognostic cloud and precipitation, are kept in grid-point space because they are not needed for any of the computations in spectral space and because the spectral transforms can violate the positivity of the transformed field, in particular for non-smooth fields.

A direct spherical harmonics transformation of a field $\Phi(\lambda, \theta)$ known at each longitude λ_l and latitude θ_k is a Fourier transformation in longitude, followed by a Legendre transformation in latitude of the Fourier coefficients Φ_m at each zonal wavenumber m :

$$\Phi_m(\theta_k) = \frac{1}{L} \sum_{l=1}^L \Phi(\lambda_l, \theta_k) e^{-im\lambda_l} \quad \Rightarrow \quad \Phi_n^m = \sum_{k=1}^K w_k \Phi_m(\theta_k) \bar{P}_n^m(\theta_k)$$

where w_k is the Gaussian weight for the latitude k and \bar{P}_n^m are the normalised associated Legendre polynomials for the zonal wavenumber m and the total wavenumber n . In spectral space, the fields are known only by their set of spectral coefficients Φ_n^m .

The discrete Fourier transform is computed numerically very efficiently by using a Fast Fourier Transform (FFT). The discrete Legendre transforms require the accurate discrete computation of the sum over the Legendre polynomials, which is accomplished by a Gaussian quadrature at the $K=2N$ special quadrature latitudes of the Gaussian grid between the two poles (the number of latitude circles between pole and equator, N , is used for the GRIB-encoded data).

The inverse discrete Legendre and Fourier transforms using a triangular spectral truncation n_{MAX} (i.e. $0 \leq n \leq n_{MAX}$ and $-n \leq m \leq n$) return the field in grid-point space, at each point of the Gaussian grid.

Recent concerns about the computational cost of the Legendre transform have been mitigated by a fast Legendre transform which exploits similarities of the associated Legendre polynomials to simplify the computations (*Wedi et al.*, 2013). Further computational acceleration can be expected from using modern hardware accelerator technologies. However, the parallel communications involved in the data transfer within transpositions from grid-point space to spectral space and back, at every time step of the model, remain a concern on future computing architectures (*Wedi et al.*, 2015).

to go around the globe at the equator. The wavelength associated with the wavenumber n is given by $2\pi a/n$, where a is the Earth's radius. The larger the wavenumber (the smaller the wavelength), the finer the scale represented by the spherical harmonic. The maximum wavenumber in the sum used to represent the meteorological fields, n_{MAX} , is the spectral truncation number of the model. The larger the truncation number, the smaller the scales potentially represented by the spectral approach. In spectral space, mathematical operations such as differentiation or integration are computed analytically using the series of spherical harmonics.

The accuracy of the transformation from grid-point space to spectral space and back is assured if the grid is a Gaussian grid, i.e. characterised by N specially determined quadrature points along a meridian between the pole and the equator, the 'Gaussian latitudes', and their associated 'Gaussian quadrature weights' used to compute the spectral coefficients (Box A). Several choices can be made to pair the maximum wavenumber of the spectral truncation, n_{MAX} , with the number of latitude circles between the pole and equator, N , which characterises the Gaussian grid.

In the current so-called linear grid, $n_{MAX} = 2N - 1$. A spectral transform using a linear grid represents the smallest wavelength $2\pi a/n_{MAX}$ by 2 grid points. Two other choices are the 'quadratic' grid and the 'cubic' grid, which represent the smallest wavelength by 3 and 4 points, respectively. The names 'linear', 'quadratic' and 'cubic' stem from the ability of the different grids to accurately represent linear, quadratic and cubic products in the equations.

The resolution of the IFS is indicated by specifying the spectral truncation n_{MAX} prefixed by the acronym TL (for triangular-linear), TQ (for triangular-quadratic), TC (for triangular-cubic) or TCo (for triangular-cubic-octahedral, see below). For example, the resolution of the current HRES is TL1279, a linear grid truncated at $n_{MAX} = 1279$.

Higher effective resolution

Until 1998, a quadratic grid was used in the IFS to avoid the aliasing resulting from the computation of the Eulerian advection. With the implementation of the semi-Lagrangian advection scheme, a linear grid was introduced to enable finer scales in the spectral representation for a given grid resolution. However, recent experience suggests that the importance of non-linear processes increases with increasing resolution, thus exacerbating the problem of aliasing and requiring computationally expensive de-aliasing filters to suppress poorly resolved or misrepresented motions (Wedi, 2014).

The notion of resolution in an NWP model is more complex than just the grid spacing. In fact, selected processes are computed at coarser resolutions (e.g. radiation) and similar techniques may be applied in future to other physical processes. Moreover, the effective resolution of a model depends on the level of implicitly or explicitly applied filtering. Such filtering can be inherent in the equations used. For example, it would be impossible to resolve

vertically propagating acoustic waves with a hydrostatic or an anelastic system of equations, whatever the time and space resolutions, as such waves are filtered by these equations. Some numerical algorithms may also be a source of significant filtering. Well-known examples are the effect of decentring in time-stepping schemes or damping in low-order interpolation. In addition, the filtering applied on boundary forcings such as the orography can be significant for the effective model resolution.

By definition, the cubic discretisation, where $n_{MAX} = N - 1$, filters wavenumbers between N and $2N$ (i.e. wavelengths between 2 and 4 times as long as the grid spacing). With such a discretisation, no numerical filter is needed apart from a small amount of numerical diffusion to eliminate any accumulation of energy at the wavenumber of the spectral truncation, and a damping layer at the model top to avoid artificial wave reflexion inside the computational domain. In addition, as shown in Figure 1, the cubic discretisation can stably support an orography with more variance in the small scales, thus providing the same spectral representation as that obtained

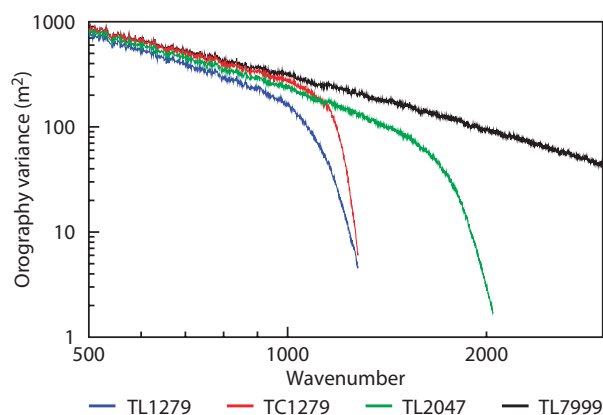


Figure 1 Variance of the orography as a function of the total wavenumber for different linear and cubic discretisations in the IFS.

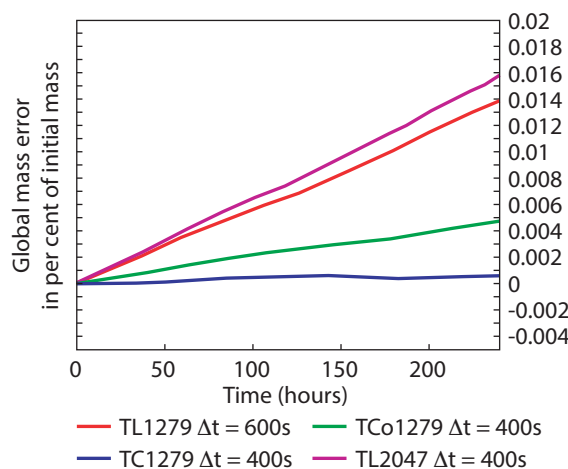


Figure 2 Global mass conservation error for 10-day forecasts at different resolutions: TL1279 with a time step of $\Delta t = 600$ s, TC1279 with $\Delta t = 400$ s, TCo1279 with $\Delta t = 400$ s. For comparison, TL2047 with $\Delta t = 400$ s is also shown. The chosen time steps are optimized for meteorological accuracy and efficiency at the given resolution.

from the original dataset for all wavenumbers almost up to the truncation limit. A cubic grid with a given truncation thus implies a higher effective resolution than a linear grid at the same and even at a higher truncation number.

As Figure 2 shows, the aliasing control required for the linear grid also has a significant impact on global mass conservation: the linear grid is associated with a steady increase in the mass conservation error over time while the cubic grid is nearly perfect without a mass fixer.

Consequently, the spring 2016 resolution upgrade (IFS cycle 41r2) will introduce a cubic spectral transform grid, with $n_{MAX} = 1279$ and $N = 1280$ latitude circles between the pole and the equator instead of $N = 640$ in the current system.

Lower computational cost

Figure 3 shows the evolution of the computational cost of a forecast as a function of the grid resolution N . The blue ‘grid factor’ bars show how the cost would grow if it increased linearly with the number of points on the grid. It can be seen that the cost of a forecast using linear or cubic discretisations grows faster than the grid factor. However, for high resolutions the cost of the global communications in the spectral transforms significantly penalizes the linear grid compared to the cubic grid.

The greater computational efficiency of the cubic grid can also be seen in Figure 4, which shows the number of forecast days that can be produced per day depending on the number of available supercomputer cores. It can be seen that cubic discretisation requires a significantly lower number of cores to achieve the same number of forecast days than linear discretisation using the same physical grid.

Octahedral reduced Gaussian grid

The choice of the spectral truncation and the number of latitude circles of the Gaussian grid is not sufficient to generate the IFS grid because it does not determine the number of grid points in the zonal direction at each latitude circle. If the same number of points is used for each latitude circle in a full Gaussian grid, the zonal resolution near the poles is substantially higher than the zonal resolution at the equator. Such a configuration generates a strong anisotropy of the discrete horizontal representation of the fields, potentially risks numerical instabilities and carries a significant computational cost due to the large number of points near the poles. For the past two decades, ECMWF has used a reduced grid (Hortal & Simmons, 1991), in which the number of points on each latitude circle is reduced towards the poles, keeping the relative grid-point distances approximately constant. This reduction lowers the number of points by approximately 30% without significant loss of meteorological accuracy in the spectral transforms.

A new method to reduce the number of grid points towards the poles has been explored for the next resolution upgrade of the IFS, both to optimize the total number of points around the globe and to introduce a regular reduction of the number of points per latitude circle

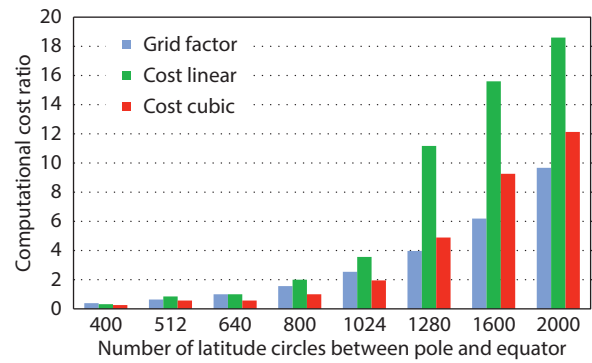


Figure 3 Computational cost relative to the current TL1279 as a function of the number of latitude circles between the pole and the equator, N . The green bars represent the relative cost of linear discretisations, the red bars that of cubic discretisations. The blue bars, shown for reference, represent the ‘grid factor’, the ratio between the number of points for a given reduced Gaussian grid divided by the about 2.1 million points at the current operational resolution TL1279 (i.e. a multiplication by about 4 of the cost for a doubling of N).

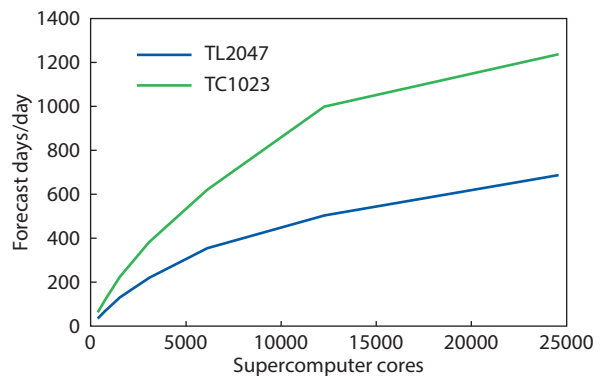


Figure 4 Computational capacity expressed in forecast days per day as a function of the number of supercomputer cores for the linear (TL2047) and the cubic (TC1023) discretisations associated with the same Gaussian grid $N = 1024$.

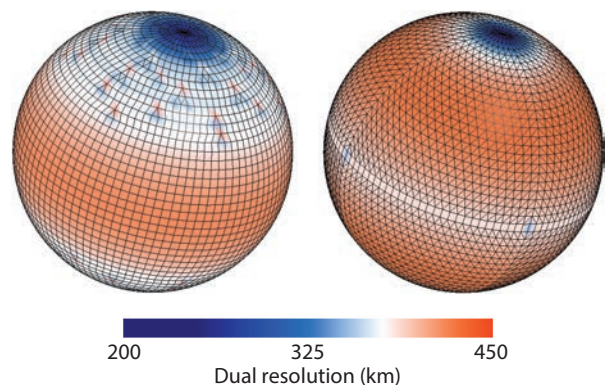
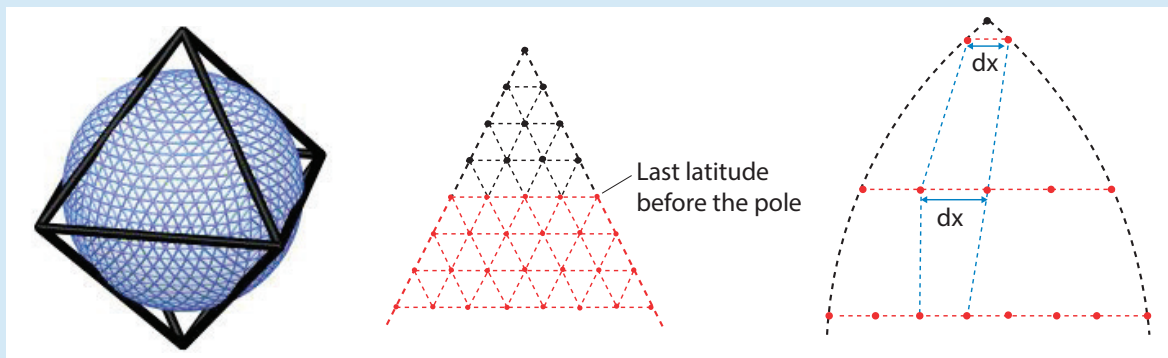


Figure 5 Primary meshes generated around the $N = 24$ reduced Gaussian grid points with 3.75 degrees (or approximate grid-point distances of 416 km). The shading represents the effective grid spacing of the median dual mesh, which is the mesh used for finite-volume computations, as explained by Smolarkiewicz et al. (2015). The shading is calculated as the square root of the local dual mesh area. The octahedral mesh (right) has a locally more uniform dual-mesh resolution than the original mesh (left). The coarse resolution is chosen for illustrative purpose only.

How to generate an octahedral reduced Gaussian grid

B

1. Imagine each hemisphere of the globe is divided into 4 quarters, with each quarter corresponding to one face of an octahedron (left).
2. Start with 20 points, i.e. 5 per quarter, at the Gaussian latitude closest to the pole (middle).
3. Add one point per quarter for each new Gaussian latitude towards the equator, i.e. 4 more points per Gaussian latitude circle.
4. Because of the curvature of the Earth, the spacing between the grid points along a latitude circle varies with the latitude. It is slightly wider in the mid-latitudes than at the equator and near the pole (right).



towards the poles. The design of this new grid is inspired by a regular triangular mapping onto an octahedron, which corresponds to a reduction of 4 points per latitude circle, one per face of the octahedron (Box B). The resulting grid is called the 'cubic-octahedral reduced Gaussian grid'.

The nominal resolution of the grid in the zonal direction is not as uniform around the globe as in the original reduced Gaussian grid (Figure 5), but the number of points per vertical level is significantly lower (for the $N = 1280$ grid, the original reduced grid has about 8.5 million points against 6.5 million for the new octahedral grid). In practice, this saves another 22% of total computation time. With the current reduced Gaussian grid, the number of points per latitude circle is constrained to be a multiple of 2, 3 and 5 by the Fast Fourier Transform (FFT) algorithm FFT992 originally developed at ECMWF by our former colleague

Clive Temperton (Temperton, 1983). The cubic-octahedral reduced Gaussian grid will be used in the IFS together with the FFT package FFTW (<http://www.fftw.org/>), which efficiently allows any number of points per latitude circle.

The spectral transform method may become computationally inefficient in the future due to the communication overhead of the global spectral transformations. To address this risk, alternative numerical methods that rely only on nearest-neighbour information are being developed at several Member State weather services and also in the context of the PantaRhei project at ECMWF (Smolarkiewicz et al., 2015). The recently investigated finite-volume module (FVM) can provide a more efficient and scalable way of computing differential operators in the IFS, but the accuracy of the approach depends also on the underlying mesh which defines

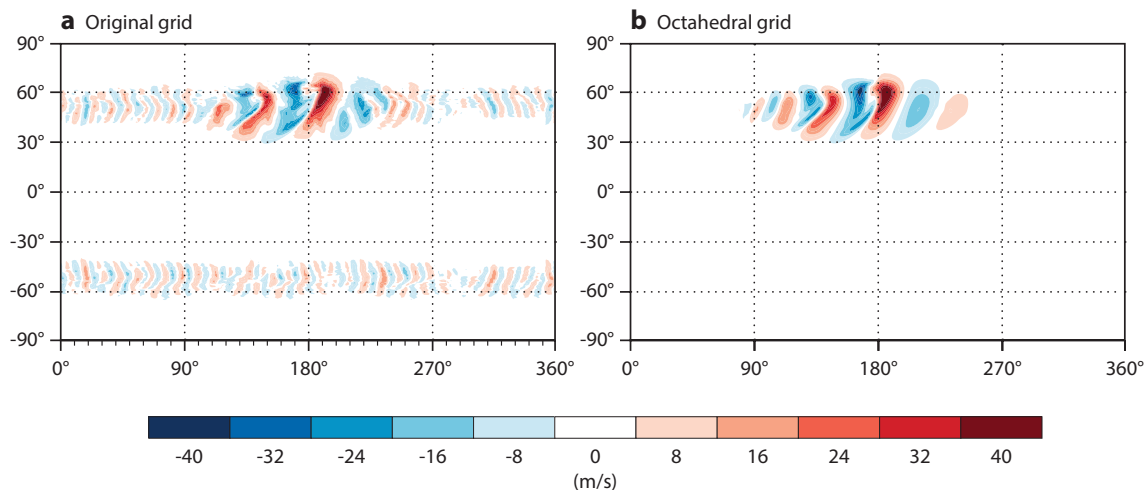


Figure 6 Idealised baroclinic wave test case using the finite-volume module of the IFS being developed at ECMWF, showing meridional wind component after 8 days of simulation for (a) the original reduced Gaussian grid and (b) the octahedral reduced Gaussian grid.

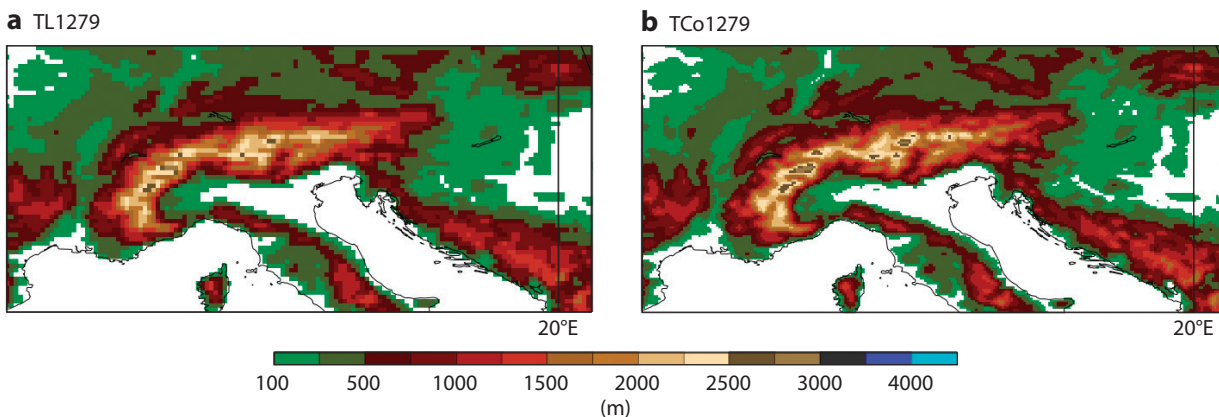


Figure 7 Representation of the Alps at (a) TL1279 and (b) TCo1279.

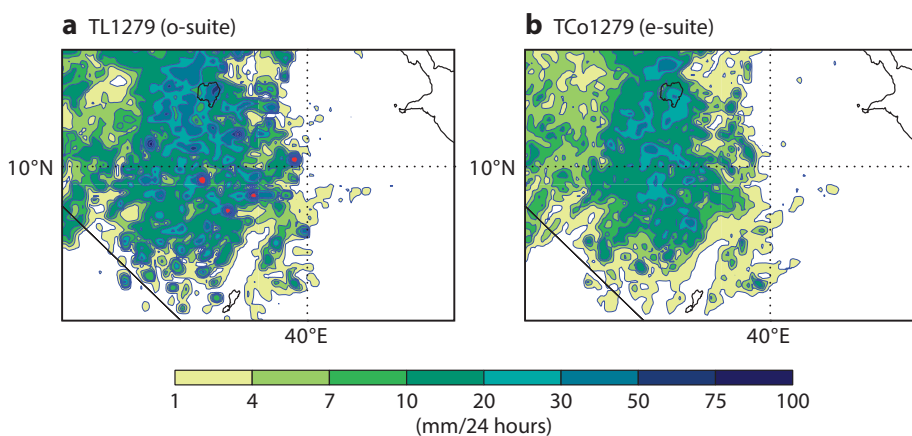


Figure 8 Accumulated 24-hour total precipitation for 24-hour forecasts starting from 15 July 2015 00 UTC in the Horn of Africa (Ethiopia, Djibouti) near Lake Tana for (a) the operational system (o-suite) at TL1279 and (b) the experimental system (e-suite) at TCo1279. The red dots in (a) show the location of spurious ‘grid-point storms’ where the predicted accumulated precipitation is larger than 100 mm.

the shape of the elementary volumes around which the computations are made. This is illustrated by results from numerical simulations of an idealised baroclinic instability using the FVM, as shown in Figure 6. Here, the more uniform mesh which is built around the grid points provided by the octahedral versus the original reduced Gaussian grid results in higher accuracy and substantially reduced unphysical flow distortions.

Summary of benefits

The cubic-octahedral spectral transform discretisation called TCo1279, with a spectral truncation at $n_{MAX} = 1279$ and a Gaussian grid with $N = 1280$ latitude circles between the pole and the equator, offers superior filtering properties at higher horizontal resolutions, an improved representation of orography, improved global mass conservation properties, and substantial efficiency gains. It also works well with more scalable, locally compact computations of derivatives and other properties that depend on nearest-neighbour information only.

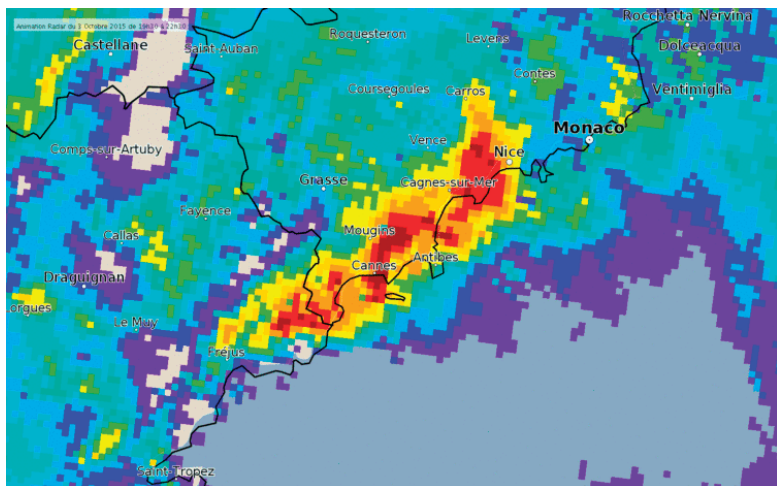
With the cubic discretisation, the filtering of the spectral orography is reduced. As shown in Figure 7, the increased variance shown in Figure 1 directly translates into a sharper representation of the resolved orographic forcing in grid-point space.

Thanks to the optimized representation of smaller resolved weather features, problems such as ‘grid-point storms’ have been completely eliminated from the new system, as illustrated by Figure 8.

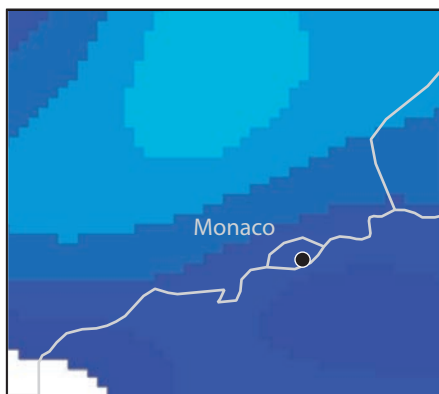
The resolution upgrade concerns not just HRES but also ensemble forecasts (ENS), the Ensemble of Data Assimilations (EDA) and the 4DVAR assimilation system. As a result of the cubic grid’s superior filtering properties, the level of filtering of the 4DVAR trajectory is now identical to that of the forecast model, and the initial analysis and evolving forecast have the same kinetic energy spectrum across the entire range of wavenumbers (not shown). Results of the evaluation being carried out in preparation for the resolution upgrade in 2016 indicate an improved effective resolution and exciting improvements to medium-range weather forecasts, as illustrated in a case study by Figure 9.

Details on the resolution upgrade can be found at <https://software.ecmwf.int/wiki/display/FCST/Horizontal+resolution+increase>

a Radar



b TL1279 (o-suite)



c TCo1279 (e-suite)

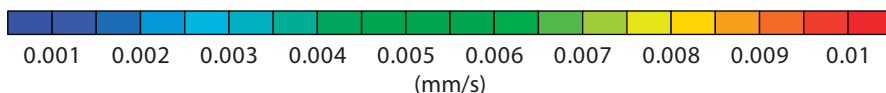
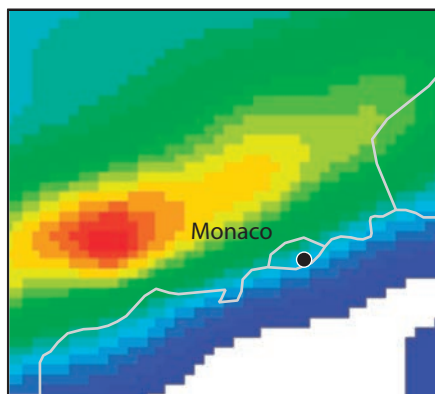


Figure 9 Total precipitation rate at 21 UTC during a severe event near Cannes on 3 October 2015 according to (a) Radar Mosaic observations, (b) a 3-hour forecast produced by the operational system (o-suite) at TL1279 and (c) a 3-hour forecast produced by the experimental system (e-suite) at TCo1279. The flash floods generated by intense and stationary convective systems during this event killed 20 people.

FURTHER READING

Eliassen, E., B. Machenhauer, & E. Rasmusen, 1970: On a numerical method for integration of the hydrodynamical equations with a spectral representation of the horizontal fields. *Report 2, Institut for Teoretisk Meteorologi, University of Copenhagen.*

Hortal, M. & A.J. Simmons, 1991: Use of reduced Gaussian grids in spectral models. *Mon. Wea. Rev.*, **119**, 1057–1074.

Orszag, S.A., 1970: Transform method for calculation of vector coupled sums: application to the spectral form of the vorticity equation. *J. Atmos. Sci.*, **27**, 890–895.

Smolarkiewicz, P., W. Deconinck, M. Hamrud, C. Kühnlein, G. Mozdzyński, J. Szmelter & N. Wedi, 2015: An all-scale, finite-volume module for the IFS. *ECMWF Newsletter No. 145*, 24–29.

Temperton, C., 1983: Self-sorting mixed-radix fast Fourier transforms. *J. Comput. Phys.*, **52**, 1–23.

Wedi, N.P., 2014: Increasing horizontal resolution in NWP and climate simulations – illusion or panacea? *Phil. Trans. R. Soc. A*, **372**, doi: 10.1098/rsta.2013.0289

Wedi, N.P., P. Bauer, W. Deconinck, M. Diamantakis, M. Hamrud, C. Kühnlein, S. Malardel, K. Mogensen, G. Mozdzyński & P.K. Smolarkiewicz, 2015: The modelling infrastructure of the Integrated Forecasting System: Recent advances and future challenges. ECMWF Research Department *Technical Memorandum No. 760.*

Wedi, N.P., M. Hamrud & G. Mozdzyński, 2013: A fast spherical harmonics transform for global NWP and climate models. *Mon. Wea. Rev.*, **141**, 3450–3461.

Using ensemble data assimilation to diagnose flow-dependent forecast reliability

MARK J RODWELL

Weather forecasting is fundamentally a probabilistic task due to the growth of unavoidable initial-state uncertainty. Moreover, the growth rates of these uncertainties can depend on the atmospheric flow so that predictability may vary from day to day. The established approach to representing uncertainty in probabilistic forecasting is to make an ensemble of forecasts, each starting from a slightly different initial state and including a different realisation of model uncertainty. A key question is how to assess the ensemble's ability to represent the flow-dependent growth of uncertainty.

Results suggest that such assessments are not easy to make at the medium range due to complications associated with error propagation and non-linear interactions. Using a specially developed ensemble reliability budget, appropriate for shorter-range assessments within the data assimilation window, these issues can be minimised and flow-dependent deficiencies in representing uncertainty can be identified. An analysis of the reliability budget can also help identify the causes of deficiencies in representing uncertainty. Results are illustrated for a flow situation where mesoscale convection is likely to occur over North America and which often results in reduced predictive skill for Europe several days later.

Forecast reliability

Figure 1 is a schematic representation of an ensemble forecast with ensemble members (blue curves) diverging in their prediction of two weather parameters (represented by the x- and y-axes) with increasing lead time t (coming out of the plane). Note that if we could produce an infinite number of ensemble members, they would describe the probability distributions depicted by the blue ellipses. A key question for numerical weather prediction is what constitutes a good ensemble forecast. Clearly users would like the ensemble distribution to be as narrow (or 'sharp') as possible in order to reduce uncertainty. However, this only makes sense if the eventual truth (black curve) lies within the ensemble distribution. More precisely, we require that the truth can be considered as another sampling of the ensemble distribution, and when this is true in general, the ensemble is said to be 'reliable'.

If we assume that forecast bias is negligible or accounted for, the next aspect of the ensemble distribution to assess in terms of reliability is its variance. The standard approach is to compare the mean ensemble variance (averaged over a set of forecast start dates) with the mean squared error of the ensemble mean ($Error^2$):

$$Error^2 = \text{EnsVar} + \text{Residual} \quad (1)$$

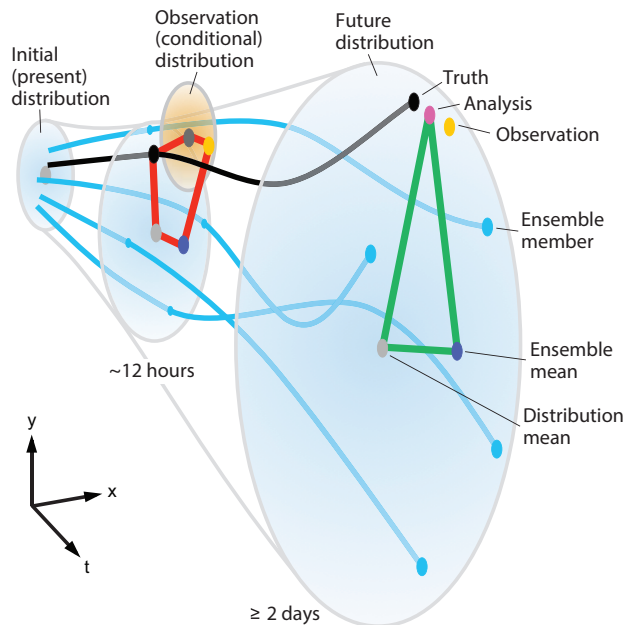


Figure 1 Schematic diagram depicting an ensemble forecast. The green and red polygons form the basis of the spread-error and 'EDA reliability budget' diagnoses of reliability, respectively. These are explained in Boxes A and B.

This equation is valid at reasonably long lead times (perhaps greater than 2 days, as depicted by the right-hand distribution in Figure 1) when forecast error is sufficiently large for analysis error to be neglected in the calculation of $Error^2$. EnsVar in (1) is the mean sample variance of the ensemble (scaled to take account of the finite size of the ensemble), and the Residual represents any ensemble variance deficit associated with deficiencies in reliability, together with sampling uncertainties (due to the limited number of forecast start dates available). For a reliable system (and assuming no analysis error) the expected value of the residual is zero. The green triangle in Figure 1 depicts the theoretical basis for this 'spread-error relationship' and, for the interested reader, its derivation is discussed further in Box A.

Using data from the ECMWF operational ensemble (ENS), Figure 2a shows northern hemisphere annual means of ensemble 'spread' and root mean square error (RMSE) of the ensemble mean (i.e. the square roots of EnsVar and $Error^2$) for 500 hPa height for the years 1996, 2005 and 2014. The reduction in RMSE at all lead times together with the better match with spread indicates substantial improvements in both sharpness and reliability over the years. Notice in particular the more realistic 'exponential' shape of the spread and error curves for 2014 over the first 5 or 6 days, which are much flatter at short ranges. These improvements have been achieved through many incremental changes to the forecasting system. These include the introduction of the Ensemble of Data

Assimilations (EDA) and the development of the ‘stochastic physics’ parametrization, which represents, amongst other things, the upscale cascade of uncertainty from subgrid scales. Improvements in the observation network and in the modelling of observation errors have also been important.

Figure 2b shows time series of the spread and RMSE for six-day forecasts for Europe from five of the world’s leading operational forecasting centres. There cannot be such a good match between spread and RMSE on a day-to-day basis. Notice, however, the agreement between centres in terms of the variation in spread. This agreement suggests flow-dependent fluctuations in underlying predictability. The main reason for making ensemble forecasts is to be able to represent these flow-dependent variations in uncertainty and predictability. For a fully reliable ensemble forecast system, the ensuing flow-dependent probabilities for a given event will match the outcome frequencies when binned and averaged over a sufficiently large sample – as displayed in ‘reliability diagrams’. Such correspondence is important to users because it allows them to make optimal decisions based on their own cost/loss models. Future steps towards such a reliable ensemble system are likely to come from more detailed flow-dependent diagnosis of model and observation error.

Difficulties in diagnosing flow-dependent reliability

Rodwell *et al.* (2012) highlighted reduced predictive skill for six-day forecasts for Europe in initial flow situations where a trough exists over the North American Rockies (e.g. as part of a Rossby wave), together with high Convective Available Potential Energy (CAPE) ahead of it. Such a situation is conducive to the formation of strong mesoscale convective systems (MCSs), which can interact with the jet

stream. The uncertainty in intensity, location and timing of these MCS features (and possibly larger-scale dynamical instabilities coupled to orography) are thought to be important for the subsequent decrease in downstream skill.

The reliability of ensemble forecasts initiated from a particular flow regime, such as the trough/CAPE pattern,

Derivation of the spread-error relationship

A

Figure 1 is a schematic representation of an ensemble forecast. The blue ellipses represent the initial and forecast distributions that one might obtain with an infinite ensemble size. For a finite ensemble size, m , the ensemble mean (dark blue dot) will not generally lie at the distribution mean (grey dot). For lead times ≥ 2 days, the analysis (pink dot) is often considered an adequate approximation for the truth (black dot).

The green triangle then shows how the (squared) error of the ensemble mean (right-hand side of the triangle) can be decomposed into the sum of the independent (squared) deviations of the truth and the ensemble mean from the distribution mean (the other two sides of the triangle). Assuming zero bias, the expected squared truth deviation can be written as the variance of the ensemble distribution plus a residual that indicates any systematic deficiency in this variance.

Because the ensemble members are independent, the expected squared ensemble-mean deviation can be written as $1/m$ times the ensemble distribution variance. The inclusion of this ensemble-mean variance, together with the desire for unbiased estimation of these terms using the available data, leads to the EnsVar term including an $\frac{m+1}{m-1}$ scaling factor in (1).

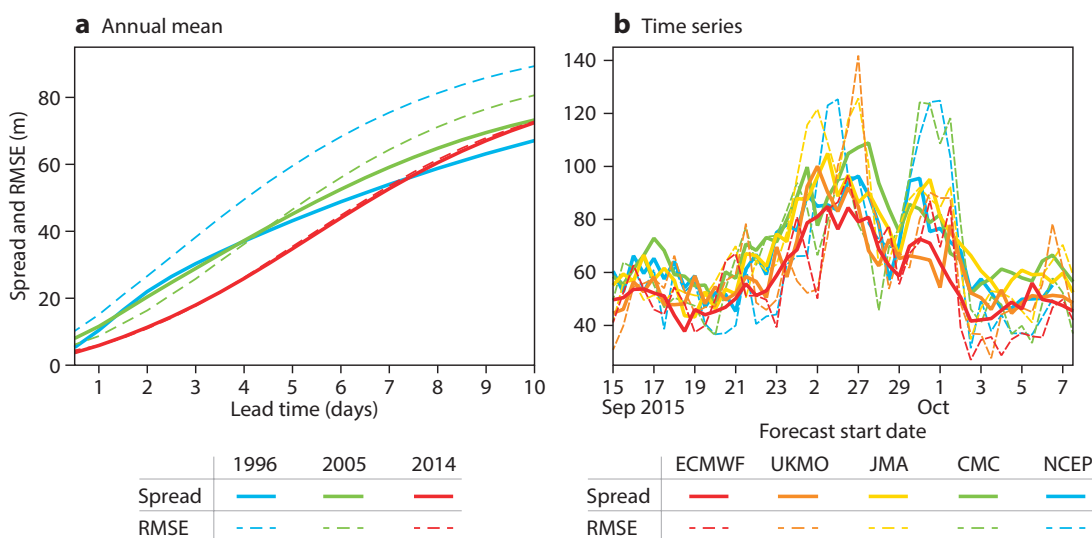


Figure 2 (a) Northern hemisphere annual means of ensemble spread and root mean square error (RMSE) of the ensemble mean for 500 hPa heights, and (b) time series of D+6 spread and RMSE for Europe from five of the world’s leading operational forecasting centres: ECMWF; UKMO (UK Met Office); JMA (Japan Meteorological Agency); CMC (Canadian Meteorological Centre); NCEP (US National Centers for Environmental Prediction). Data retrieved from the TIGGE archive and interpolated to a 2.5° regular grid, with RMSE calculated relative to each centre’s own analysis. The northern hemisphere includes latitudes north of 30°N, and Europe is defined here as 12.5°W–42.5°E, 35°N–75°N.

can also be assessed using (1). Figure 3 shows, for geopotential at 200 hPa (the jet stream level), the terms in (1) for a composite of the 54 cases during the period 19 November 2013 – 12 May 2015 (when cycle 40r1 of ECMWF’s Integrated Forecasting System was operational) for which the initial conditions closely matched the trough/CAPE pattern, using the same method as in *Rodwell et al.* (2012). Large mean squared errors ($Error^2$) at forecast day 1 (D+1) can be seen over the Great Lakes region of North America (Figure 3a), associated with MCS activity. These errors are reasonably well predicted, on average, by the ensemble variance (EnsVar, Figure 3b). As the lead time increases, this error/spread signal is seen to propagate east across the North Atlantic (D+3 in Figure 3d,e and D+5 in Figure 3g,h). Notice in particular the large $Error^2$ at D+5 close to Western Europe (Figure 3g). This error is more than 15% greater than for the ‘non-trough/CAPE’ composite (consisting of the remaining about 1,000 forecasts, not shown), but the variance is actually slightly smaller than in the non-trough/CAPE composite (not shown). The right-hand panels in Figure 3 show the Residual ($Error^2$ minus EnsVar). The positive residual near Western Europe at D+5 (Figure 3i) suggests that the ensemble variance might be too small, but this is not statistically significant at the 5% level (saturated colours indicate statistical significance). The statistically significant negative residuals seen elsewhere in Figure 3 are generally not specific to the trough/CAPE situation.

The conclusion here is that there is broad agreement over the medium range between spread and error in this

flow-specific situation, but it is difficult to identify the causes of residual differences. The crossing of the blue ensemble trajectories in Figure 1 represents the fact that errors are growing within a non-linear regime, interacting and dispersing through the action of teleconnections and waves in general. It is these effects that make it inherently difficult to assess flow-dependent ensemble reliability in the medium range, and even harder to identify the causes of any lack of reliability. By the same argument, it is also these effects that make it difficult to use off-line calibration techniques to improve flow-dependent reliability. Such improvements need to be made within the model itself and require more precise diagnostic tools.

The EDA reliability budget

In order to facilitate a more local and flow-dependent assessment of reliability, it proves useful to consider much shorter lead times (about 12 hours, as depicted by the central distribution in Figure 1), when errors are growing within a more linear regime and have not had so much time to interact or to disperse geographically. In anticipation of the development of a more seamless EDA/ENS system in the future, it makes sense to apply this test to the background forecasts of the EDA. These background forecasts include the most relevant part of the stochastic physics parametrization – the stochastic perturbation of physical tendencies (SPPT) scheme – and avoid potential complications associated with the re-centring and singular vector perturbations presently used in the initialisation of the ENS. At these short lead times, uncertainty in

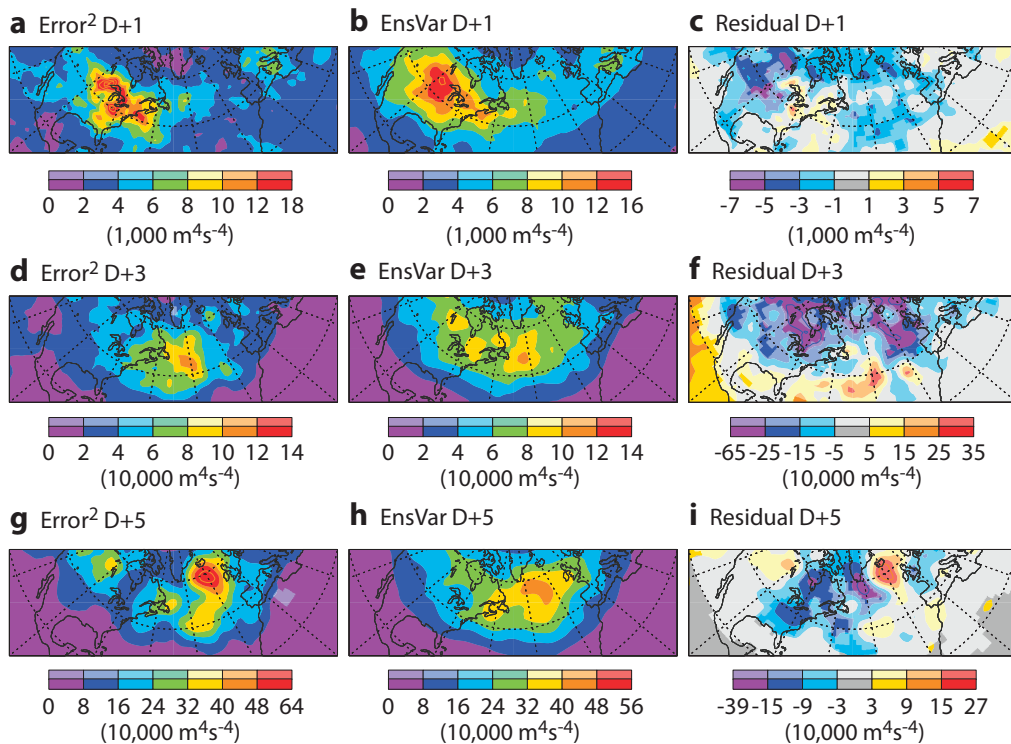


Figure 3 Terms in the spread-error relationship (1) for 200 hPa geopotential based on the ‘trough/CAPE’ composite for (a)–(c) D+1; (d)–(f) D+3; and (g)–(i) D+5. Statistical significance at the 5% level (from a null hypothesis of zero) is indicated by saturated colours and is deduced using a Student’s t-test applied to the set of 54 forecasts.

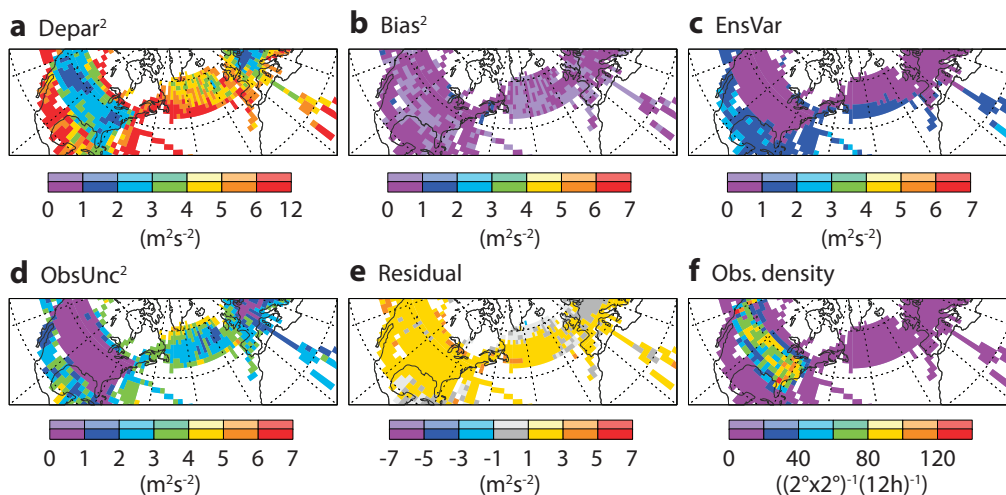


Figure 4 Panels (a) to (e) show the terms in the ‘EDA reliability budget’ (2) applied to 200 hPa zonal winds for the non-trough/CAPE composite. The data used are aircraft observations between 185 and 215 hPa that are actively assimilated, and the corresponding winds interpolated from the EDA background forecasts. Panel (f) shows the density of aircraft observations assimilated within the EDA control. To reduce noise, an average of at least one observation per 2°x2° grid box per 12-hour analysis cycle is required for the budget to be plotted. Values significantly different from zero at the 5% level are shown with saturated colours.

our knowledge of the truth cannot be neglected. We could incorporate an EDA analysis variance term into our reliability test to take account of this aspect, but we choose to work in observation space since the modelling of observation error (depicted by the orange ellipse in Figure 1) represents a more foundational aspect of the data assimilation process. Because observation errors cannot be neglected, we talk about ‘departures’ from observations rather than ‘errors’ from the truth. The new ‘EDA reliability budget’, the basis of which is depicted graphically by the red pentagon in Figure 1 and which is discussed further in Box B, is a decomposition of the mean squared departures of the form

$$\text{Depar}^2 = \text{Bias}^2 + \text{EnsVar} + \text{ObsUnc}^2 + \text{Residual} \quad (2)$$

As before, EnsVar is the scaled sample variance, but now of the EDA background forecasts. ObsUnc² is the sample variance of the observation errors as modelled within the assimilation system. Bias² is the square of the estimated remaining bias of the model relative to the observations after the application of observation bias correction methods. Note that bias is sometimes neglected in the traditional spread-error assessment, but this risks the possibility that ensemble variance is erroneously inflated to achieve agreement with the squared error. The Residual quantifies the ensemble variance deficit (plus any deficiencies in the modelling of observation error). Non-zero values in either the Bias² term or the Residual are indicative of reliability deficiencies. Further details of the development of this budget are given in Rodwell *et al.* (2015).

To obtain a better understanding of the meaning of the terms in (2), and of the equation’s utility in the assessment of flow-dependent ensemble reliability, it is useful to consider some examples. There are two key questions to answer: Is the EDA reliability budget able to identify

statistically significant reliability deficiencies when it is analysed for a particular flow regime? If so, then what are these deficiencies?

Assessment of flow-dependent reliability

The EDA reliability budget will be computed for the trough/CAPE composite. First, however, it is useful to consider EDA reliability in a less flow-dependent context by computing the budget for the non-trough/CAPE composite. Figure 4 shows, for the non-trough/CAPE composite, the terms in (2) together with the observation density, for 200 hPa zonal wind speed, based on aircraft measurements and their corresponding values in the EDA background. Aircraft observations are numerous over central North America at this cruising altitude (Figure 4f) and, indeed, they are particularly influential in the data assimilation system. Observation uncertainty (Figure 4d) is computed from the independent observation errors assigned within the EDA. When averaged onto a 2°x2° grid, the observation uncertainty is naturally smallest

Derivation of the EDA reliability budget

B

At short lead times, uncertainty in our observational knowledge of the truth cannot be ignored. The red pentagon in Figure 1 shows how the spread-error relationship can be extended to include bias and random observation error. The departure of the ensemble mean from the observation is now written in terms of the remaining four sides of the pentagon. Assuming constant bias, these four terms are either independent or uncorrelated, so the expected square of the decomposition again simply involves the squares of the individual differences. Estimation with the available data then leads to the ‘EDA reliability budget’ (2).

where the observation density is largest. The EDA reliability budget decomposes the squared departure term (Depar^2 ; Figure 4a) into contributions from the bias (Bias^2 ; Figure 4b), ensemble variance (EnsVar ; Figure 4c), observation uncertainty (ObsUnc^2 ; Figure 4d) and a Residual term (Figure 4e). The spatial structure of the Depar^2 term in the non-trough/CAPE composite largely follows that of the observation uncertainty. There is also a contribution from the ensemble variance, and possibly a more uniform offset associated with the bias. Figure 4e shows, however, that there is a small but statistically significant residual term, which suggests some general deficiency in reliability. This is not investigated further here because we are interested in flow-dependent reliability.

Figure 5 shows the EDA reliability budget terms for the trough/CAPE composite. Comparison of Figure 5 with Figure 4 shows increased departures around the Great Lakes in the trough/CAPE composite. Larger departures are to be expected because of the strong (and less predictable) convection liable to be taking place. The increased ensemble variance indicates more forecast uncertainty in this region. Notice, however, that this increase does not fully account for the increased departures, and consequently the Residual term (note the different shading interval) increases markedly too in the region associated with MCS activity and has roughly twice the magnitude of the ensemble variance. One possibility is that the ObsUnc^2 term does not increase sufficiently in these convective situations. However, aircraft wind observations are thought to be quite accurate (they are assimilated without bias correction) and they are probably dense enough in this region (≥ 60 per $2^\circ \times 2^\circ$ grid box per 12 hours, and with little change in density) to rule out an increase in representativeness errors for the upper-tropospheric wind field. Hence it is likely that the background variance is strongly deficient in these trough/CAPE (and MCS) regimes. From a diagnostic development point of view, the key result here is that the EDA reliability budget is able to identify flow-dependent deficiencies in reliability. Next we consider what this budget can tell us about the root causes of reliability deficiencies.

Causes of flow-dependent reliability problems

The ensemble variance deficit following trough/CAPE situations could be due to deficiencies in stochastic physics – either in magnitude or formulation. Note, for example, that the ‘Stochastic Kinetic Energy Backscatter’ (SKEB) scheme is not included in the EDA background. The relatively low resolution of the background (T399, corresponding to a horizontal resolution of about 50 km) may also necessitate stronger stochastic physics in these mesoscale convection situations. Such a conclusion about deficiencies in stochastic physics is consistent with the results of *Rodwell et al. (2015)*, who showed that the EDA reliability budget (applied to mid-tropospheric temperatures observed by AMSU-A satellite microwave channel 5) was able to highlight regional deficiencies in variance that were sensitive to changes in stochastic physics. For example, positive residuals in convective regions were deteriorated by turning off the stochastic physics. At the same time, negative residuals within subtropical anticyclone regions (where the mid-tropospheric meteorology is largely characterised by time-mean descent and clear-sky radiative cooling) were improved by turning off the stochastic physics.

There are, however, other possible causes for the residual seen in the MCS example. For example, ‘analysis tendency and increment’ diagnostics (*Rodwell & Palmer, 2003*) suggest that, for the trough/CAPE situation, the net physical heating within MCS events is placed too low in the atmosphere (not shown). One can hypothesise that this may weaken the interaction in the momentum field between the jet stream and the MCS outflow, which could be another reason for the apparent lack of ensemble variance. Hence one can imagine situations where reliability deficiencies are associated with flow-dependent systematic error.

Although ruled out in the example shown, the EDA reliability budget is also sensitive to observation error assignment. This can be considered useful because a good modelling of observation error is also important for the reliable

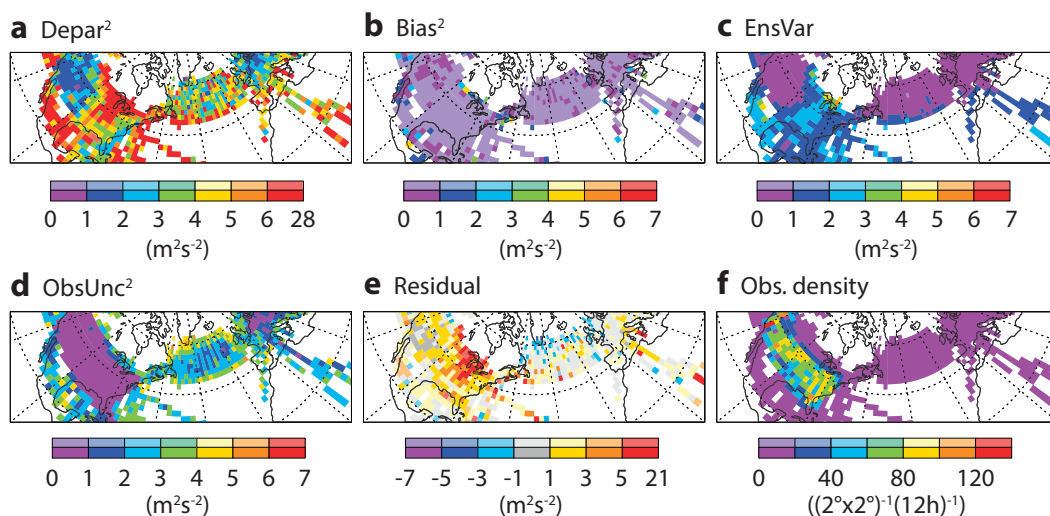


Figure 5 As Figure 4, but for the trough/CAPE composite.

initialisation of ensemble forecasts. There can be situations where the residual term is most clearly associated with the assignment of observation error variances, for example in regions where residuals of different signs are found for different observation types and are thus less likely to be associated with ensemble variance errors. While these observation error variances are already estimated by a variety of means, such as ‘Desroziers statistics’, Rodwell *et al.* (2015) demonstrated, for surface pressure observations over the oceans from ships and buoys, that the EDA reliability budget may also be useful in this regard. It is likely that there will be situations where deficiencies in both stochastic physics and the assignment of observation error are important. In such situations, additional information might be required to resolve the ambiguity.

In some situations, the bias term in (2) can also highlight errors in the ensemble distribution. For example, the EDA reliability budget for the AMSU-A satellite microwave channel 5 indicated significant biases off the west coast of South America, possibly associated with undetected shallow cloud in the observations. While (observation) bias is legitimately assumed to have been accounted for in the data assimilation process, it is clearly worth including this term in (2) from a diagnostic perspective.

Summary and outlook

A necessary condition for ‘reliable’ ensemble forecasts is that ensemble variance accurately represents the flow-dependent growth of initial and model uncertainties. A key question is how to diagnose deficiencies in this ensemble variance. For a particular initial flow known to be associated with reduced predictability, the traditional spread-error relationship was not able to identify the causes of medium-range variance deficiencies. This is partly because, by the medium range, errors are growing within a non-linear regime, interacting and dispersing. To minimise such issues, it is useful to look at the shorter timescales associated with the background forecasts of the Ensemble of Data Assimilations (EDA).

At these shorter lead times, as with data assimilation itself, uncertainties in our observational knowledge of the truth must be accounted for. This leads to the derivation of an ‘EDA reliability budget’ (Rodwell *et al.*, 2015) that decomposes mean squared departures (of the background ensemble mean relative to the observations) into squared-bias, ensemble-variance and observation-uncertainty terms, together with a residual that closes the budget. Results show that the residual (and bias) terms of the EDA reliability budget can identify regional and flow-dependent deficiencies in reliability. Although ambiguities may still arise, it is hoped that the EDA reliability budget will be a useful tool to diagnose our modelling of the non-linear fluid-dynamical/physical system (including, in future, the development of stochastically formulated physical parametrizations), our modelling of the observation operators (radiative transfer etc.), and our modelling of observation error.

For reduced forecast uncertainty, it is also important to increase the sharpness of probabilistic forecasts through reduced initial uncertainty. Subject to the ensemble being reliable, sharpness is chiefly addressed through improved observational information and data assimilation methods and can therefore be largely addressed separately from the modelling aspects associated with reliability.

ECMWF’s proposed new strategy foresees the development of a more seamless EDA/ENS system, as depicted schematically in Figure 1. The use of a consistent model (same physics, stochastic physics and resolution) and consistent initialisation of the EDA background and ENS will mean that EDA reliability results like those presented here should facilitate improvements in medium-range reliability too. As lead time increases through the medium range and beyond, slower processes such as those associated with the land surface, ocean and sea ice also become important in the forecast. By examining reliability at all lead times, and representing uncertainties close to their sources, it may be possible to ensure that errors associated with these slower processes are also well represented.

FURTHER READING

Desroziers, G., L. Berre, B. Chapnik & P. Poli, 2005: Diagnosis of observation background and analysis-error statistics in observation space. *Quart. J. R. Meteorol. Soc.*, **131**, 3385–3396, doi: 10.1256/qj.05.108.

Isaksen, L., J. Hasler, R. Buizza & M. Leutbecher, 2010: The new ensemble of data assimilations. *ECMWF Newsletter No. 123*, 17–21.

Leutbecher, M. & T.N. Palmer, 2008: Ensemble forecasting. *J. Comp. Phys.*, **227**, 3515–3539, doi: 10.1016/j.jcp.2007.02.014.

Rodwell, M.J., L. Magnusson, P. Bauer, P. Bechtold, C. Cardinali, M. Diamantakis, E. Källén, D. Klocke, P. Lopez, T. McNally, A. Persson, F. Prates & N. Wedi, 2012: Characteristics of occasional poor medium-range forecasts for Europe. *ECMWF Newsletter No. 131*, 11–15.

Rodwell, M.J., S.T.K. Lang, N.B. Ingleby, N. Bormann, E. Hólm, F. Rabier, D.S. Richardson & M. Yamaguchi, 2015: Reliability in ensemble data assimilation. *Quart. J. R. Meteorol. Soc.*, doi: 10.1002/qj.2663.

Rodwell, M.J. & T.N. Palmer, 2003: Using numerical weather prediction to assess climate models. *Quart. J. R. Meteorol. Soc.*, **133**, 129–146, doi: 10.1002/qj.23.

ECMWF's new data decoding software ecCodes

ENRICO FUCILE, SÁNDOR KERTÉSZ,
SYLVIE LAMY-THÉPAUT, SHAHRAM NAJM

BUFR and GRIB are binary data formats developed by the World Meteorological Organization (WMO) to enable the worldwide exchange of meteorological data through the WMO's Global Telecommunication System. BUFR (Binary Universal Form for the Representation of meteorological data) is a flexible format mainly used to encode observations, although it can also represent forecast data. GRIB (General Regularly-distributed Information in Binary form) is designed to encode data produced by numerical weather prediction models.

The vast majority of data processed at ECMWF are either in BUFR or GRIB format. Therefore, developing effective software to decode and encode data in these formats is extremely important to facilitate scientific research, build a robust forecasting system and create tools for visualisation and other processing purposes.

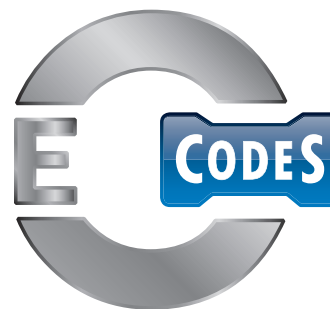
ecCodes is a new software package developed at ECMWF to enable decoding and encoding of meteorological data in BUFR or GRIB format using a single, simple interface. It will replace ECMWF's current GRIB decoder/encoder, GRIB-API, and current BUFR decoder/encoder, BUFRDC.

Key/value approach

Since 2011, GRIB-API has been the only software library used to decode and encode GRIB at ECMWF. It is used in several Member States and has been made available as open source software to WMO and the scientific community. GRIB-API has successfully attracted a wide user community because of the simplicity of its programming interface based on a key/value approach. In this approach, any piece of information, such as 'latitude of first grid point', is associated with a key name, such as 'latitudeOfFirstGridPoint'. The association with key names hides the complexity of the underlying GRIB format. Users can access the data using just a few 'get' and 'set' functions and the semantics of the key names. This paradigm has proven to be so effective in facilitating user access to GRIB data that several users have requested a similar software library for BUFR to benefit from the key/value approach.

This is why ECMWF has developed ecCodes, which provides a single programming interface to access both BUFR and GRIB in a consistent manner without any need for detailed knowledge of the binary format. A beta version of ecCodes has been released on the ECMWF website and is available as open source software under the Apache 2.0 license.

ecCodes is based on the key/value approach developed for GRIB-API while extending the key name semantics to cater for the complexity of the BUFR format. The GRIB encoding and decoding features of ecCodes are inherited from GRIB-API and are unchanged. We can think of ecCodes as being GRIB-API with extended decoding/encoding capabilities to



deal with BUFR and other formats. ecCodes also inherits its design from GRIB-API: a decoding engine written in C and a set of text definition files. The definition files contain the decoding rules for each data type in a specific language interpreted by the decoding engine.

BUFR format

WMO developed BUFR to replace the Traditional Alphanumeric Codes (TAC) used since the fifties to continuously exchange meteorological data on a worldwide basis. BUFR is a binary format suitable for the exchange of large datasets, while TAC were designed to be readable directly by humans and to be exchanged by telex.

To provide flexibility in the definition of new types of meteorological datasets, BUFR was developed as a Table Driven Code Form (TDCF), with a stable core of encoding rules on the one hand and external tables that are subject to change on the other. WMO provides regular updates of the external tables to describe new datasets. BUFR decoding or encoding software does not require any change to be able to access new datasets defined with new tables available on the WMO website. Using external tables made BUFR flexible, but it has the drawback that users continually have to refer to the tables to interpret the data. The complexity of the rules and the lack of software providing a high-level view of BUFR data make it very difficult for scientific users to make sense of the data without having some knowledge of the underlying binary representation.

Descriptors are the elementary building blocks of BUFR syntax and semantics. They identify the meaning and decoding rule for associated pieces of information (Box A). Each descriptor has a six-digit identifier (such as '012063'). The list of allowed descriptors with their meaning is provided in external tables maintained by WMO, and updates are provided twice a year.

Combining descriptors to build a meaningful data structure requires the knowledge of complex rules. On the other hand, the syntax and semantics of descriptors is flexible enough to allow the representation of any kind of meteorological dataset.

For a full description of the BUFR format, we refer the interested reader to the *WMO Manual on Codes* (2014).

ecCodes key names

The design of ecCodes aims to provide a semantics layer hiding the underlying complexity of BUFR. This is achieved by giving key names to all descriptors (Box A) and providing the software library with 'get' and 'set' functions to access and modify the information associated with each descriptor. For example, the value associated with the descriptor '012063' can be accessed with the key name 'brightnessTemperature' using the following syntax:

```
value=codes_get(bufnr, 'brightnessTemperature')
```

In this case, users do not have to know the descriptor code and can transparently access the value using the key name. Moreover, the units of this parameter are available using special syntax applied to the key name:

```
units=codes_get
(bufnr, 'brightnessTemperature->units')
```

Units are provided as an attribute of all key names. Other attributes are: 'code', which refers to the BUFR descriptor code value ('012063' in this case); and width, scale and reference, which are related to the binary representation of the data. Many other attributes may be available in a sufficiently complex data structure.

Providing key names has the advantage that the user software clearly references each physical quantity, improving maintainability compared to the use of the obscure descriptor code value, whose semantics is mapped externally in a table. Using key names to retrieve information also helps to avoid potential confusion

BUFR descriptors

A

We can think of BUFR messages as a continuous bit-stream made up of a sequence of octets (1 octet = 8 bits). Each message is composed of five sections. The first three sections contain some headers and the last section marks the end of the message. The information is encoded in sections 3 and 4. Section 3 is a list of descriptors, each of which occupies two octets and is made up of three parts: F (2 bits), X (6 bits) and Y (8 bits). Section 4 contains the data encoded as described in section 3 with the descriptors.

The descriptor F-X-Y uniquely identifies the meaning and decoding rule for the associated piece of information.

There are four types of descriptors:

- F=0 (Element Descriptor). Each element is a single piece of information with a floating point, integer or string value.
- F=1 (Replication Operator). These are used to repeat a sequence of descriptors several times.
- F=2 (Operator Descriptor). These define operations on other descriptors.
- F=3 (Sequence Descriptor). These define sequences of descriptors of any type.

stemming from the versioning of the external tables. This is because the content of the tables may differ from version to version and the data producer can define their own local tables (although this practice is discouraged by WMO). Therefore, the decoding software should take care of the table version management and provide users with the piece of information required in their specific application. For example, if the user software is retrieving a piece of information associated with the descriptor '012063', this descriptor could have different meanings in different table versions and could be linked to a variable which is different from the required 'brightnessTemperature'. ecCodes sorts out the semantics and provides users with the appropriate piece of information regardless of the BUFR descriptor code value.

In order to provide the necessary support for ecCodes management of BUFR tables, we have reviewed ECMWF local tables and organised the WMO tables into a database. A snapshot of this comprehensive BUFR table database

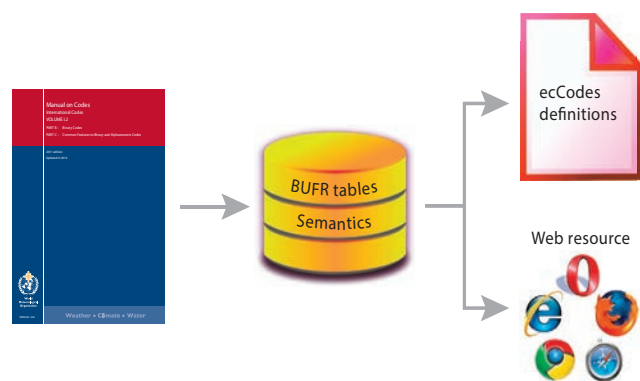


Figure 1 The BUFR tables from the WMO Manual on Codes are inserted into a database and the key names are added. The database is used to create the definitions used by ecCodes for decoding/encoding and to populate web pages for documentation.

Useful web resources

B

ecCodes home page:
software.ecmwf.int/wiki/display/ECC/ecCodes+Home

ecCodes documentation page:
software.ecmwf.int/wiki/display/ECC/Documentation

A snapshot of ECMWF's BUFR table database:
software.ecmwf.int/wiki/display/ECC/BUFR+tables

New BUFR format validator page:
apps.ecmwf.int/codes/bufr/validator

GRIB-API home page:
software.ecmwf.int/wiki/display/GRIB/Home

WMO International Codes web page:
<http://www.wmo.int/pages/prog/www/WMOCodes.html>

BUFR data encoding

`bufr_filter` is a command-line tool providing a simple language to quickly decode and encode data in BUFR format. The `bufr_filter` is applying the instructions written in a text file to an input BUFR file, and it can write the encoded BUFR data to an output file.

Below we give the example of the content of a filter instruction file to encode aircraft report data. In this case only the 'set' instruction (equivalent to the 'codes_set' instruction in Fortran or Python) is used to modify the data and produce a new BUFR dataset:

```
# choosing the tables versions
set masterTablesVersionNumber=24;
set localTablesVersionNumber=0;
# data in compressed format
set compressedData=1;
# number of reports to be encoded
set numberOfSubsets=10;
# choosing the aircraft reports template
set unexpandedDescriptors={311001};
# setting data values
set windSpeed = {10,5.3,3.4,4.5,5.6,6,6,32,22,15.2};
set airTemperature = {273.0,300.1,273.0,300.1,273.0,300.1,273.0,300.1,273.0,300.3};
#setting more data
...
# packing
set pack=1;
# writing the data
write;
```

If we write the previous instructions in a file named 'instructions.filter', 'bufr_filter' can be used in the following way to produce the new aircraft report data (output.bufr) from a generic BUFR dataset used as input (input.bufr):

```
bufr_filter -o output.bufr instructions.filter input.bufr
```

The simplicity of the `bufr_filter` syntax, built on top of the `ecCodes` key name semantics, provides a powerful tool for BUFR data processing.

is available from the ECMWF software website (Box B). In the database, a key name is defined for each descriptor, and the content of the database is used to create the text definition files which are used by `ecCodes` to decode the BUFR data. Tools have been developed to create `ecCodes` text definition files from the database and to publish the same content on the ECMWF software website, ensuring consistency between `ecCodes` and the information accessible from the website (Figure 1).

Key name syntax

`ecCodes` does not only provide a semantic mapping to the BUFR descriptors. It also applies the syntactic rules of the descriptors to provide users with an understandable data structure. To achieve this, a simple syntax for the key names has been developed.

The simple example of using a key name to access a piece of information (an element) is not always applicable because the data structure can be complex and the same key name can appear several times in different branches of the data tree. We may for example have a dataset in which the physical quantity of interest is 'backscatter' and we

have several satellite instrument beams in the dataset from which we can get the backscatter. `ecCodes` provides two options in this situation.

1. Access by rank

The element is accessed using the rank in the data tree structure:

```
value=codes_get(bufr, '#3#backscatter')
```

This returns the backscatter value at rank three in the data structure.

2. Access by condition

The element is accessed by specifying a condition, such as:

```
value=codes_get(bufr, '/beamIdentifier=3/
backscatter')
```

This returns the value of backscatter for the data tree branch where 'beamIdentifier' has the value 3.

The attributes for the key name 'backscatter' accessed by rank or condition are still accessible with the attribute syntax, as follows:

```
units=codes_get(bufnr, '#3#backscatter->units')
```

or

```
units=codes_get(bufnr, '/beamIdentifier=3/backscatter->units')
```

Some of the BUFR features are very complex and difficult to understand for users who are not experts at binary encoding. One of the most complicated features is the bitmap, which links two different elements in the same BUFR dataset. This is useful when a value such as confidence or other quality information needs to be associated with a data item. ecCodes makes the association and exposes the associated values as attributes of the data item. As an example, for a 'temperature' element, we can access the percent confidence as:

```
value=codes_get(bufnr, 'temperature->percentConfidence')
```

As for any other key, we can also get the units of percent confidence as:

```
units=codes_get(bufnr, 'temperature->percentConfidence->units')
```

Users can access extra information regarding the physical parameter using simple attribute syntax and do not have to know the details of how this information is dealt with at BUFR coding level. They can thus focus on the scientific aspect of data processing without needing to master the details of BUFR coding.

Access by rank or condition and the attribute notation are the only syntax rules currently available in ecCodes, and

BUFR validator

The purpose of the validator is to verify the compliance of data in BUFR format with the specifications in the [WMO Manual on Codes](#).

Use the file box to upload your BUFR file

No file selected.

The file size is limited to 2 megabytes.

The file scat.bufr contains 1 message and complies with the specifications in the WMO Manual on Codes.

- Header
- Data
 - centre: 99
 - subCentre: 0
 - softwareIdentification: 801
 - satelliteIdentifier: 4
 - satelliteInstruments: 190
 - directionOfMotionOfMovingObservingPlatform: [294, 294, ..., 297, 297] deg
 - year: 2012 a
 - month: 11 mon
 - day: 2 d
 - hour: 0 h
 - minute: [0, 0, ..., 1, 1] min
 - second: [58, 58, ..., 7, 7] s
 - latitude: [-86.0699, -86.0489, ..., -72.8618, -72.7537] deg
 - longitude: [-28.5502, -26.9506, ..., 36.7414, 36.8399] deg
 - index: 14
 - code: 006001 mber
 - scale: 500000000
 - reference: -18000000 m
 - width: 26PerUnitLengthOfAtmosphere: 2.3e-9 dB/m
 - beamCollocation: 1
 - beamIdentifier: 1
 - beamIdentifier: 1
 - radarIncidenceAngle: [63.96, 63.5, ..., 62.79, 63.23] deg
 - antennaBeamAzimuth: [126.79, 125.16, ..., 150.77, 150.67] deg
 - backscatter: [-14.3, -13.06, ..., -15.22, -15.53] dB
 - radiometricResolutionNoiseValue: [7.4, 5.3, ..., 11.5, 11.8] %
 - ascatKpEstimateQuality: 0
 - ascatSigma0Usability: 0
 - ascatUseOfSyntheticData: 0

Figure 2 The new BUFR validator, based on the ecCodes decoder, provides a tree view of a BUFR dataset.

they are considered sufficient to navigate the data tree and obtain the desired information. They provide easy access to BUFR data and a programming interface hiding the details of the binary code.

Another advantage of defining syntax rules for key names is that they can be used in any supported language, such as Python, Fortran 90 or C, in a consistent way. The result of obtaining information associated with a key name in Python will be the same as in Fortran 90 or C, and the functions in the three languages are very similar.

BUFR encoding

ecCodes can also be used to encode data into BUFR format. This involves two steps: defining the data structure and filling up the structure with values. A BUFR data structure is encoded as a sequence of descriptors. ecCodes provides the key name 'unexpandedDescriptors' to create the desired sequence. After setting this key name, ecCodes creates a skeleton BUFR data structure with all elements of information set to 'missing'. At this point users can set the values using the relevant key names to finalise the BUFR dataset.

If we aim to produce aircraft reports, we can get the descriptor for this type of data from the WMO table, which is '311001', and write the following instruction:

```
codes_set(buf, 'unexpandedDescriptors',  
          311001)
```

This instruction will produce a BUFR dataset with a data section ready for data value encoding. We can now set values for all the parameters present in the data structure (e.g. 'airTemperature', 'windDirection', 'windSpeed') by just using the function 'codes_set' as many times as necessary (Box C).

Programming languages and tools

Python, Fortran 90 and C are the programming languages available in ecCodes. The use of the key name library is very similar in all of them. 'Get' and 'set' functions are used to access information through key names. The key name syntax is the same in all three languages, and this makes it easier to switch from one to the other. The library is designed to be easily extended to other languages. We may add support for more languages in the future if there is enough interest and resources to make the appropriate bindings.

A set of command line tools is also provided to help users perform common tasks in shell scripts. The tools are similar to the GRIB-API tools and have similar behaviour. We suggest starting with the 'bufilter' command, which provides a quick way to test key syntax and to experiment with 'setting' and 'getting' information from a dataset. An example of the use of 'bufilter' is provided in Box C and more are available from the ecCodes documentation page.

Another useful tool is 'bufr_dump', which provides a JSON dump of the content of a BUFR dataset. JSON is the JavaScript Object Notation and is a standard widely used in web applications. Many JSON viewers are also available

as web browser plugins. This format is very convenient for inspecting data and allows users to have a view of and navigate the data structure before using ecCodes functions or tools to access the data. The suggested way of working with ecCodes is for users to inspect the data using bufr_dump and a JSON viewer, familiarise themselves with the key names in the dataset using bufr_filter, and eventually write a Python or a Fortran program to make use of the data.

For many years, ECMWF has provided a web page where users can verify whether a BUFR dataset conforms to the WMO standard. This web application was based on the BUFRDC decoder. With the migration to a new website, it has been decided to provide a new version of the validator based on the new ecCodes decoder. This is the first application where we have experimented with creating a JSON dump of the BUFR data. We make use of the output of bufr_dump directly in a JavaScript application to provide a tree view of the dataset (Figure 2). Although the JSON format is excellent for a first look at the data and for interactive navigation, for performance reasons we advise using the library calls in the available languages or the command line tools for data processing purposes.

Release schedule

ecCodes has been built to provide a user-friendly decoder to access data in BUFR and GRIB format. It is based on the key/value approach adopted for the first time in GRIB-API, and it is going to replace GRIB-API and the current BUFR decoder BUFRDC. GRIB-API will be replaced with minimal impact on the user code as most GRIB-API functions and tools will be provided in ecCodes with the same behaviour. BUFRDC will be replaced at a different pace since there are big differences to ecCodes. However, the simplification and improved maintainability provided by ecCodes in the user software should encourage rapid migration to the new decoding library as soon as ecCodes is provided in its full release version. The version of ecCodes that is currently available for download from the ECMWF website is a beta release and cannot be used in an operational environment. The availability of the full release version, which is expected for 2016, will be announced on the ecCodes home page and via the ecCodes mailing list.

Documentation and examples are available on the ecCodes documentation web page, and we suggest interested readers familiarise themselves with ecCodes by going through the examples and contact software.support@ecmwf.int if they encounter any issues.

FURTHER READING

WMO, 2014: Manual on Codes. *WMO Publication No. 306*.

TAC Representatives, Computing Representatives and Meteorological Contact Points

Member States	TAC Representatives	Computing Representatives	Meteorological Contact Points
Austria	Mr G. Tschabuschnig	Mr M. Langer	Dr A. Schaffhauser
Belgium	Mr D. Gellens	Mrs L. Frappez	Mr T. Vanhamel
Croatia	Ms B. Matjacic	Mr V. Malović	Ms B. Matjacic
Denmark	Mr C. Simonsen	Mr T. Lorenzen	Mr H. Gisselø
Finland	Mr J. Hyrkkänen	Mr M. Aalto	Mr A. Vähämäki
France	Mr F. Lalaurette	Miss C. Allouache	Ms N. Girardot
Germany	Dr D. Schröder	Dr E. Krenzien	Mr T. Schumann
Greece	Mr A. Emmanouil	Mr. N. Andritsos	Mr A. Lalos Ms C. Petrou
Iceland	Mr T. Hervarsson	Mr V. Gislason	Mrs E. B. Jónasdóttir
Ireland	Ms S. O'Reilly	Mr T. Daly	Mr G. Fleming
Italy	Lt. Col. L. Torrasi	Mr L. Facciorusso	Mr A. Di Diodato
Luxembourg	Mrs M. Reckwerth	Mrs. M. Reckwerth	Mrs. M. Reckwerth
Netherlands	Mr R. van Lier Mr T. Moene	Mr H. de Vries	Mr J. Diepeveen
Norway	Mrs C. Husum Vold	Mr K. Steinar Dale	Ms V. Wauters Thyness
Portugal	Ms V. Costa	Mr B. Anjos	Mr N. M. Moreira
Serbia	Ms L. Dekic	Mr N. Mijatović	Mr B. Bijelic
Slovenia	Mr J. Jerman	Mr P. Hitij	Mr A. Hrabar
Spain	Mr P. del Rio	Mr R. Corredor	Mr. A. Alcazar
Sweden	Mr F. Linde	Mr R. Urrutia	Mr F. Linde
Switzerland	Dr P. Steiner	Mr A. Koster	Mr E. Müller
Turkey	Mr M. Fatih Büyükkasapbaşı	Mr M. Emre Yakut	Mr A. Guser
United Kingdom	Mr I. Forsyth	Mr W. Roseblade	Mr I. Forsyth
Co-operating States			
Bulgaria	Mr E. Etropolski	Mr E. Etropolski	Mrs A. Stoycheva
Czech Republic	Ms A. Trojakova	Mr K. Ostatnický	Mr F. Sopko
Estonia	Mr A. Männik Mr A. Luhamaa	Mr H. Kaukver	Mrs T. Paljak
The former Yugoslav Republic of Macedonia	Mr O. Romevski	Mr B. Sekirarski	Ms N. Aleksovska
Hungary	Mr I. Ihász	Mr I. Ihász	Mr I. Ihász
Israel	Mr I. Rom	Mr V. Meerson	Mr N. Stav
Latvia	Mr J. Braucs	Mr J. Braucs	Ms A. Niznika
Lithuania	Mrs V. Auguliene	Mr M. Kazlauskas	Mrs V. Raliene
Montenegro	Mr A. Marčev	Mr A. Marčev	Ms S. Pavicevic
Morocco	Mr H. Haddouch	Mr M. Jidane	Mr K. Lahlal
Romania	Mrs A. Ristici	Mr C. Ostroveanu	Ms M. Georgescu
Slovakia	Mr J. Vivoda	Dr O. Španiel	Dr M. Benko Dr J. Csaplár
Observers			
EUMETSAT	Mr A. Ratier	Dr S. Elliott	
WMO	Mr P. Taalas		

ECMWF Council and its committees

The following provides some information about the responsibilities of the ECMWF Council and its committees. More details can be found at:

<http://www.ecmwf.int/about/committees>

Council

The Council adopts measures to implement the ECMWF Convention; the responsibilities include admission of new members, authorising the Director-General to negotiate and conclude co-operation agreements, and adopting the annual budget, the scale of financial contributions of the Member States, the Financial Regulations and the Staff Regulations, the long-term strategy and the programme of activities of the Centre.



President Prof Dr Gerhard Adrian (Germany)

Vice President Dr Miguel Miranda (Portugal)

Policy Advisory Committee (PAC)

The PAC provides the Council with opinions and recommendations on any matters concerning ECMWF policy submitted to it by the Council, especially those arising out of the four-year programme of activities and the long-term strategy.



Chair Mrs Marianne Thyrring (Denmark)

Vice Chair Mr Arni Snorrason (Iceland)

Finance Committee (FC)

The FC provides the Council with opinions and recommendations on all administrative and financial matters submitted to the Council and shall exercise the financial powers delegated to it by the Council.



Chair Mr Marko Viljanen (Finland)

Vice Chair Mr Mark Hodkinson (United Kingdom)

Scientific Advisory Committee (SAC)

The SAC provides the Council with opinions and recommendations on the draft programme of activities of the Centre drawn up by the Director-General and on any other matters submitted to it by the Council. The 12 members of the SAC are appointed in their personal capacity and are selected from among the scientists of the Member States.



Chair Prof Sarah Jones (Deutscher Wetterdienst)

Vice Chair Jón Egill Kristjánsson (Norway)

Technical Advisory Committee (TAC)

The TAC provides the Council with advice on the technical and operational aspects of the Centre including the communications network, computer system, operational activities directly affecting Member States, and technical aspects of the four-year programme of activities.



Chair Mr Jean-Marie Carrière (France)

Vice Chair Dr Philippe Steiner (Switzerland)

Advisory Committee for Data Policy (ACDP)

The ACDP provides the Council with opinions and recommendations on matters concerning ECMWF Data Policy and its implementation.



Chair Mr Frank Lantsheer (Netherlands)

Vice Chair Mr Soren Olufsen (Denmark)

Advisory Committee of Co-operating States (ACCS)

The ACCS provides the Council with opinions and recommendations on the programme of activities of the Centre, and on any matter submitted to it by the Council.



Chair Mr Martin Benko (Slovakia)

Vice Chair Mr Priidik Lagemaa (Estonia)

ECMWF Calendar 2016

Jan 25–29	Computer User Training Course: HPC Facility Cray XC30
Feb 1–5	Training Course for Trainers, Training Champions: Use and Interpretation of ECMWF Products
Feb 8–12	Training Course: Use and Interpretation of ECMWF Products
Feb 22–26	Computer User Training Course: Introduction for New Users/MARS
Mar 2	Workshop on verification measures
Mar 3	Technical Advisory Committee subgroup on verification measures
Mar 7–8	Workshop for MARS Administrators
Mar 7–11	NWP Training Course: Data Assimilation
Mar 14–18	EUMETSAT/ECMWF NWP SAF Training Course: Assimilation of Satellite Data
Apr 11–14	ECMWF/WWRP Workshop on Model Uncertainty
Apr 11–15	NWP Training Course: Advanced Numerical Methods for Earth System Modelling
Apr 18	EUMETSAT Data Policy Group – Switzerland
Apr 19	Advisory Committee for Data Policy – Switzerland
Apr 20	ECOMET Working Group
Apr 25	Policy Advisory Committee
Apr 25–27	ERA-CLIM2 Review and Progress Meeting
Apr 26–27	Finance Committee
May 9–13	NWP Training Course: Predictability and Ocean–Atmosphere Ensemble Forecasting

May 16–20	NWP Training Course: Parametrization of Subgrid Physical Processes
May 17–18	Security Representatives' Meeting
May 18–20	Computing Representatives' Meeting
May 31 – Jun 1	Technical Advisory Committee subgroup on verification measures
Jun 6–8	Using ECMWF's Forecasts (UEF)
Jun 30 – Jul 1	Council
Sep 5–9	Annual Seminar
Sep 12–16	Workshop on Drag Processes and Links to Large-Scale Circulation
Sep 26–30	Computer User Training Course: Data Analysis and Visualisation using Metview
Sep 29–30	Working Group for Co-operation between European Forecasters (WGCEF)
Oct 3–6	Workshop on Numerical and Computational Methods for Simulation of All-Scale Geophysical Flows
Oct 13–14	Technical Advisory Committee
Oct 24–28	Workshop on High-Performance Computing in Meteorology
Nov 7–11	Workshop on Tropical Modelling and Assimilation
Nov 15–17	EUMETSAT Satellite Application Facility on Climate Monitoring (CM SAF) Workshop
Nov 21–25	UERRA General Assembly
Nov 29–30	ECOMET GA and EUMETNET Assembly
Dec 1–2	Council

Contact information

ECMWF, Shinfield Park, Reading, Berkshire RG2 9AX, UK

Telephone National 0118 949 9000

Telephone International +44 118 949 9000

Fax +44 118 986 9450

ECMWF's public website <http://www.ecmwf.int/>

E-mail: The e-mail address of an individual at the Centre is firstinitial.lastname@ecmwf.int. For double-barrelled names use a hyphen (e.g. j-n.name-name@ecmwf.int).

Problems, queries and advice	Contact
General problems, fault reporting, web access and service queries	calldesk@ecmwf.int
Advice on the usage of computing and archiving services	advisory@ecmwf.int
Queries regarding access to data	data.services@ecmwf.int
Queries regarding the installation of ECMWF software packages	software.support@ecmwf.int
Queries or feedback regarding the forecast products	forecast_user@ecmwf.int

ECMWF publications

(see <http://www.ecmwf.int/en/research/publications>)

Technical Memoranda

- 767 **Lu, Q., H. Lawrence, N. Bormann, S. English, K. Lean, N. Atkinson, W. Bell & F. Carminati:** An evaluation of FY-3C satellite data quality at ECMWF and the Met Office. *November 2015*
- 766 **Geer, A.:** Significance of changes in medium-range forecast scores. *October 2015*
- 765 **Haiden, T., M. Janousek, P. Bauer, J. Bidlot, M. Dahoui, L. Ferranti, F. Prates, D.S. Richardson & F. Vitart:** Evaluation of ECMWF forecasts, including 2014–2015 upgrades. *November 2015*
- 764 **Herman, M., Z. Fuchs, D. Raymond & P. Bechtold:** Convectively coupled Kelvin Waves: From linear theory to global models. *October 2015*
- 763 **Sandu, I., P. Bechtold, A. Beljaars, A. Bozzo, F. Pithan, T.G. Shepherd & A. Zadra:** Impacts of parameterized orographic drag on the Northern Hemisphere winter circulation. *October 2015*
- 762 **Dutra, E., I. Sandu, G. Balsamo, A. Beljaars, H. Freville, E. Vignon & E. Brun:** Understanding the ECMWF winter surface temperature biases over Antarctica. *November 2015*
- 760 **Wedi, N.P., P. Bauer, W. Deconinck, M. Diamantakis, M. Hamrud, C. Kühnlein, S. Malardel, K. Mogensen, G. Mozdzyński, P.K. Smolarkiewicz:** The modelling infrastructure of the Integrated Forecasting System: Recent advances and future challenges. *November 2015*
- 759 **Rodwell, M.J., L. Ferranti, T. Haiden, L. Magnusson, J. Bidlot, N. Bormann, M. Dahoui, G. De Chiara, S. Duffy, R. Forbes, E. Hólm, B. Ingleby, M. Janousek, S.T.K. Lang, K. Mogensen, F. Prates, F. Rabier, D.S. Richardson, I. Tsonevsky, F. Vitart & M. Yamaguchi:** New Developments in the Diagnosis and Verification of High-Impact Weather Forecasts. *November 2015*

ERA Report Series

- 22 **Milan, M. & L. Haimberger:** Predictors and grouping for variational bias correction of radiosonde. *November 2015*

Index of newsletter articles

This is a selection of articles published in the *ECMWF Newsletter* series during recent years.

Articles are arranged in date order within each subject category.

Articles can be accessed on the ECMWF public website – <http://www.ecmwf.int/en/research/publications>

	No.	Date	Page		No.	Date	Page
NEWS							
Alan Thorpe's legacy at ECMWF	146	Winter 2015/16	2	El Niño set to strengthen but longer-term trend uncertain	143	Spring 2015	3
Forecasting flash floods in Italy	146	Winter 2015/16	3	Upbeat mood as MACC project draws to a close	143	Spring 2015	4
Forecast performance 2015	146	Winter 2015/16	5	Forecasts for US east coast snow storm in January 2015	143	Spring 2015	6
Tropical cyclone forecast performance	146	Winter 2015/16	7	New training module for Metview software	143	Spring 2015	7
Monitoring the 2015 Indonesian fires	146	Winter 2015/16	8	Benefits of statistical post-processing	143	Spring 2015	8
Visualising data using ecCharts: a user perspective	146	Winter 2015/16	9	Modelling the Quasi-Biennial Oscillation	143	Spring 2015	8
Forecasts aid flood action in Peru during El Niño	146	Winter 2015/16	10	Warm conditions continue from 2014 into 2015	143	Spring 2015	9
Calibrating river discharge forecasts	146	Winter 2015/16	12	The role of hindcast length in assessing seasonal climate predictability	143	Spring 2015	11
CERA-20C production has started	146	Winter 2015/16	13	Stochastic workshop explores simulation of forecast model uncertainty	143	Spring 2015	12
Migration to new ECMWF website is complete	146	Winter 2015/16	15	Piotr Smolarkiewicz granted Poland's top academic title	143	Spring 2015	13
Software updates in preparation for model cycle 41r2	146	Winter 2015/16	16	Annual Seminar proceedings published	143	Spring 2015	13
Forty years of improving global forecast skill	145	Autumn 2015	2	ECMWF Copernicus Services – Open for Business	142	Winter 2014/15	2
Predicting this year's European heat wave	145	Autumn 2015	4	Additional clustering time-periods available for dissemination and in MARS	142	Winter 2014/15	3
ECMWF meets its users to discuss forecast uncertainty	145	Autumn 2015	6	Forecast performance 2014	142	Winter 2014/15	4
Trans-polar transport of Alaskan wildfire smoke in July 2015	145	Autumn 2015	8	Membership of the Scientific Advisory Committee	142	Winter 2014/15	5
Ensemble of Data Assimilations applied to atmospheric composition	145	Autumn 2015	10	Serbia becomes ECMWF's 21st Member State	142	Winter 2014/15	6
Using the OpenIFS model to describe weather events in the Carpathian Basin	145	Autumn 2015	11	Flow-dependent background error covariances in 4DVAR	142	Winter 2014/15	7
ECMWF helps ESO astronomers peer deep into space	145	Autumn 2015	12	Forecasts for a fatal blizzard in Nepal in October 2014	142	Winter 2014/15	8
Surface verification in the Arctic	145	Autumn 2015	14	New blog for software developers	142	Winter 2014/15	9
ECMWF assimilates data from two new microwave imagers	145	Autumn 2015	14	Recognition of ECMWF's role in THORPEX	142	Winter 2014/15	9
Improved spread and accuracy in higher-resolution Ensemble of Data Assimilations	145	Autumn 2015	15	Update on migration to BUFR for radiosonde, surface and aircraft observations at ECMWF	142	Winter 2014/15	10
A first look at the new ecFlow user interface	145	Autumn 2015	16	Sharing knowledge about climate data	142	Winter 2014/15	11
Third OpenIFS user meeting held at ECMWF	144	Summer 2015	2	Copernicus Climate Change and Atmosphere Monitoring Services	141	Autumn 2014	2
New model cycle launched in May	144	Summer 2015	4	Recent cases of severe convective storms in Europe	141	Autumn 2014	3
EU approves scalability projects	144	Summer 2015	5	Licensing ECMWF products	141	Autumn 2014	5
ECMWF forecasts for tropical cyclone Pam	144	Summer 2015	6	Closing the GRIB/NetCDF gap	141	Autumn 2014	6
Rescuing satellite data for climate reanalysis	144	Summer 2015	8	Peter Janssen awarded the EGU Fridtjof Nansen Medal for 2015	141	Autumn 2014	7
Over 100 attend NWP training programme	144	Summer 2015	10	MACC-III forecasts the impact of Bardarbunga volcanic SO ₂	141	Autumn 2014	8
ECMWF hosts Eumetcal workshop on training	144	Summer 2015	10	ERA-20C goes public for 1900–2010	141	Autumn 2014	9
New S2S database complements TIGGE archive	144	Summer 2015	11				
Week of events to explore visualisation in meteorology	144	Summer 2015	12	VIEWPOINT			
ECMWF-run Copernicus services get new websites	144	Summer 2015	13	Living with the butterfly effect: a seamless view of predictability	145	Autumn 2015	18
ECMWF makes its mark at geosciences conference	144	Summer 2015	14	Decisions, decisions...!	141	Autumn 2014	12
Work on Copernicus Climate Change Service under way	143	Spring 2015	2				

	No.	Date	Page		No.	Date	Page
Using ECMWF's Forecasts: a forum to discuss the use of ECMWF data and products	136	Summer 2013	12	Improving ECMWF forecasts of sudden stratospheric warmings	141	Autumn 2014	30
Describing ECMWF's forecasts and forecasting system	133	Autumn 2012	11	Improving the representation of stable boundary layers	138	Winter 2013/14	24
COMPUTING				Interactive lakes in the Integrated Forecasting System	137	Autumn 2013	30
ECMWF's new data decoding software ecCodes	146	Winter 2015/16	35	Effective spectral resolution of ECMWF atmospheric forecast models	137	Autumn 2013	19
Supercomputing at ECMWF	143	Spring 2015	32	Breakthrough in forecasting equilibrium and non-equilibrium convection	136	Summer 2013	15
SAPP: a new scalable acquisition and pre-processing system at ECMWF	140	Summer 2014	37	Convection and waves on small planets and the real Earth	135	Spring 2013	14
Metview's new user interface	140	Summer 2014	42	Global, non-hydrostatic, convection-permitting, medium-range forecasts: progress and challenges	133	Autumn 2012	17
GPU based interactive 3D visualization of ECMWF ensemble forecasts	138	Winter 2013/14	34				
RMDCN – Next Generation	134	Winter 2012/13	38				
METEOROLOGY				PROBABILISTIC FORECASTING & MARINE ASPECTS			
OBSERVATIONS & ASSIMILATION				Using ensemble data assimilation to diagnose flow-dependent forecast reliability	146	Winter 2015/16	29
GEOWOW project boosts access to Earth observation data	145	Autumn 2015	35	Have ECMWF monthly forecasts been improving?	138	Winter 2013/14	18
CERA: A coupled data assimilation system for climate reanalysis	144	Summer 2015	15	Closer together: coupling the wave and ocean models	135	Spring 2013	6
Promising results in hybrid data assimilation tests	144	Summer 2015	33	20 years of ensemble prediction at ECMWF	134	Winter 2012/13	16
Snow data assimilation at ECMWF	143	Spring 2015	26	Representing model uncertainty: stochastic parametrizations at ECMWF	129	Autumn 2011	19
Assimilation of cloud radar and lidar observations towards EarthCARE	142	Winter 2014/15	17	METEOROLOGICAL APPLICATIONS & STUDIES			
The direct assimilation of principal components of IASI spectra	142	Winter 2014/15	23	Improvements in IFS forecasts of heavy precipitation	144	Summer 2015	21
Automatic checking of observations at ECMWF	140	Summer 2014	21	New EFI parameters for forecasting severe convection	144	Summer 2015	27
All-sky assimilation of microwave humidity sounders	140	Summer 2014	25	The skill of ECMWF cloudiness forecasts	143	Spring 2015	14
Climate reanalysis	139	Spring 2014	15	Calibration of ECMWF forecasts	142	Winter 2014/15	12
Ten years of ENVISAT data at ECMWF	138	Winter 2013/14	13	Twenty-five years of IFS/ARPEGE	141	Autumn 2014	22
Impact of the Metop satellites in the ECMWF system	137	Autumn 2013	9	Potential to use seasonal climate forecasts to plan malaria intervention strategies in Africa	140	Summer 2014	15
Ocean Reanalyses Intercomparison Project (ORA-IP)	137	Autumn 2013	11	Predictability of the cold drops based on ECMWF's forecasts over Europe	140	Summer 2014	32
The expected NWP impact of Aeolus wind observations	137	Autumn 2013	23	Windstorms in northwest Europe in late 2013	139	Spring 2014	22
Winds of change in the use of Atmospheric Motion Vectors in the ECMWF system	136	Summer 2013	23	Statistical evaluation of ECMWF extreme wind forecasts	139	Spring 2014	29
New microwave and infrared data from the S-NPP satellite	136	Summer 2013	28	Flow-dependent verification of the ECMWF ensemble over the Euro-Atlantic sector	139	Spring 2014	34
Scaling of GNSS radio occultation impact with observation number using an ensemble of data assimilations	135	Spring 2013	20	iCOLT – Seasonal forecasts of crop irrigation needs at ARPA-SIMC	138	Winter 2013/14	30
ECMWF soil moisture validation activities	133	Autumn 2012	23	Forecast performance 2013	137	Autumn 2013	13
Forecast sensitivity to observation error variance	133	Autumn 2012	30	An evaluation of recent performance of ECMWF's forecasts	137	Autumn 2013	15
FORECAST MODEL				Cold spell prediction beyond a week: extreme snowfall events in February 2012 in Italy	136	Summer 2013	31
Reducing systematic errors in cold-air outbreaks	146	Winter 2015/16	17	The new MACC-II CO2 forecast	135	Spring 2013	8
A new grid for the IFS	146	Winter 2015/16	23	Forecast performance 2012	134	Winter 2012/13	11
An all-scale, finite-volume module for the IFS	145	Autumn 2015	24	Teaching with OpenIFS at Stockholm University: leading the learning experience	134	Winter 2012/13	12
Reducing surface temperature errors at coastlines	145	Autumn 2015	30	Uncertainty in tropical winds	134	Winter 2012/13	33
Atmospheric composition in ECMWF's Integrated Forecasting System	143	Spring 2015	20	Monitoring and forecasting the 2010-11 drought in the Horn of Africa	131	Spring 2012	9
Towards predicting high-impact freezing rain events	141	Autumn 2014	15				



Newsletter | Number 146 – Winter 2015/16

European Centre for Medium-Range Weather Forecasts

www.ecmwf.int